UNIVERSITÀ DI PISA

Corso di Laurea Magistrale in Fisica della Materia

Realization of networks of nanofibers and study of their laser emission properties

Relatore:

Prof. Dario Pisignano

Laureando:

Sofia Papa

Correlatore:

Dott. Andrea Camposeo

Anno accademico 2022/2023

Contents

1 Introduction **3**

2 Properties and Fabrication Technologies of Random and Nanofiber Lasers **7**

2.1 Random Lasing: Properties and Applications 7

2.1.1 Nanofiber Lasers 7

2.1.2 Random Lasers 9

2.1.3 Network Lasers 10

2.1.4 Applications of Random Lasers 10

2.2 3D Printing and Electrospinnig Technologies 14

2.2.1 Stereolithography 15

2.2.2 3D Printing by Extrusion 16

2.2.3 Direct Ink Writing 16

2.2.4 Fused Deposition Modeling 20

2.2.5 Electrospinning 21

2.3 3D Printing Combined with Electrospinning 24

2.3.1 Examples of Systems Combining 3DP and ES 27

3 Materials and Methods **34**

3.1 DIW 34

3.1.1 Materials 34

3.1.2 Bioplotter 36

3.1.3 Results 38

3.2 Materials for FDM and ES 39

3.2.1 Vetroalfa 39

3.2.2 PLACTIVE^{TM} 40

3.2.3 Graphene Composite 41

3.2.4 Polyvinyl-alcohol (PVA) 42

3.2.5 Rhodamine B 42

3.3 Setup for FDM and ES 43

3.3.1 Fused Deposition Modeling 3D printer 44
3.3.2 Electrospinning System 47
3.4 Methods for Samples Characterization 47
3.4.1 Optical Microscope 47
3.4.2 Integrating Sphere 49
3.4.3 Characterization of Electrical Properties 49
3.4.4 Characterization of Lasing Properties 51

4 Experimental Results **53**
4.1 3D Printing Implementation 53
4.1.1 3D Printing of Vetroalfa 54
4.1.2 3D Printing of Graphene/PLA composite 56
4.1.3 3D Printing of nanocomposite PLA 59
4.2 Morphological Analysis of Electrospun Nanofibers 60
4.3 Combination of 3DP and ES Processes 68
4.4 Morphological Analysis of Hybrid Samples 70
4.5 Optical Properties of Hybrid Samples 77

5 Conclusion and Perspectives **84**

1 Introduction

Since their invention in 1960, lasers have had an increasing impact in different scientific and technological fields such as industrial manufacturing, additive manufacturing, metrology and medicine [1]. Conventional lasers consist of an active light-emitting medium, a pumping system and an optical cavity. In these systems, light emitted by the active medium upon suitable pumping is amplified by stimulated emission. The main features of the resulting laser radiation are a high degree of monochromaticity, coherence, directionality and brightness [2].

Recently novel laser systems have been introduced (known as random lasers) in which light amplification occurs through light diffusion in a disordered medium with optical gain [3]. Unlike conventional lasers, the emission of random lasers is a consequence of multiple scattering [3], and they typically feature multimode emission. In addition, the spatial coherence of the emission of random lasers has been reported to be much lower than that of a conventional laser [4]. These peculiar features make random lasers suitable for applications in super-resolution spectroscopy [5] and speckle-free imaging [6].

Among the various complex materials exploited so far for the realization of random lasers, organic nanofibers (NFs) and nanowires (NWs) are very promising, because in such (almost 1D) nanostructures the light diffusion and light amplification properties can be designed by the morphology of the individual fibers and the architecture of the arrays made of them [7]. To achieve random lasing, polymer NFs have to be doped with either molecules or nanomaterials that provide optical gain, while the emitted light can be guided and amplified through the single NFs and diffused by the disordered assembly of the NFs. This allows multimode laser emission to be observed [7] in arrays of nanofibers and, more recently, a nanophotonic network

laser has been reported in which the lasing properties are tailored by the topology of the nanofiber network [8].

The most widely used technique to realize nanofibers is electrospinning (ES) [9], a process that exploits the electric field between a metallic needle and collector, to extrude a viscoelastic polymeric solution. For random laser applications, the integration of ES with 3D printing technologies is expected to expand the control on the architecture of the deposited fiber arrays and the properties of the realized complex laser devices. The objective of this work is the realization of hybrid samples made of 3D structures and arrays of light-emitting nanofibers with random lasing properties. Typically, the combination of ES and 3D printing technologies is achieved by using two separate and independent equipment for 3D printing and ES, respectively [10, 11, 12]. Moreover, various systems have been designed and realized, which combine these technologies in a single equipment. In such systems, the printing and electrospinning processes can be operated either in a serial manner [13, 14] or concomitantly by exploiting a unique printing/electrospinning head [15, 16, 17].

The apparatus built for the scope of this thesis has two separate printing and ES heads, while the sample platform is moved automatically from one to the other depending on the features of the samples to be realized. The system was made by modifying an Anycubic i3 mega fused deposition modeling (FDM) 3D printer and adding a dedicated ES station.

In the first part of the work, the two printing stations were separately studied and the corresponding samples characterized. Various materials were tested for the FDM process. To obtain optically transparent samples, the Vetroalfa polymer filament was used. Arrays of randomly oriented NFs can be deposited on top of the structures made by Vetroalfa. To explore other fiber assemblies, a composite material (polylactic-acid, PLA, doped with graphene) was used, which allows for 3D printing of electrically conductive components and for the control of the mutual alignment of the deposited fibers. Moreover, 3D structures were made with PLACTIVE^{TM} polymer, a nanocomposite material with antimicrobial properties.

For the realization of NFs, solutions with different concentrations of poly(vinyl alcohol) (PVA) in distilled water were electrospun. NFs with diameters $<$200 nm were

made by using PVA with molecular weight (Mw) of 13.000-23.000 g/mol. In order to obtain NFs with larger diameter, PVA with Mw of 85.000-124.000 g/mol was used and NFs with an average diameter of 460 ± 170 nm were obtained.

In the second part of the work, the deposition of NFs was optimized on top of 3D printed structures. To this aim, the graphene/polymer composite material was used. Rhodamine B (RhB, emission at about 587 nm) was added to PVA/water solution as the chromophore, in order to obtain electrospun fluorescent NFs. A solution made of 14% PVA/water weight/weight (w/w) and 1% w/w RhB/PVA was electrospun. With the optimized process parameters, nanofibers with an average diameter of 530 ± 180 nm were obtained. Then, samples with fibers suspended through a 3D printed frame were realized. This geometry was selected because it allows a better confinement of light emitted by the dye in the electrospun fibers, due to the refractive index contrast between the PVA polymer and the surrounding air. To this aim, electrospun fibers were deposited on top of a printed frame (20mm×20mm×3mm) with a 4mm hole in the centre. This sample was made with different density of nanofibers. Finally, the optical properties of the samples were investigated by optical pumping with a Nd:YAG laser. Through such measurements the threshold excitation fluence can be determined. Lasing thresholds of about 2.7 mJ cm^{-2} were measured. Moreover, a dependence of the lasing emission spectrum on the spatial intensity profile of the excitation beam was observed.

The thesis is structured as follows:

a) In Chapter 2 the properties of lasers made of NFs are presented. Afterwards, the main 3D printing techniques are described, with a focus on FDM. Finally the state of the art regarding the combination of 3D printing and ES technologies is presented.

b) In Chapter 3 the materials used for 3D printing and electrospinning, the experimental setups and the techniques used for samples characterization are illustrated. The results of the fabrication of elastomeric filaments are also reported.

c) Chapter 4 presents the results of the morphological analysis of samples obtained by FDM and ES.

d) The results of the characterization of morphological and optical properties of

hybrid fluorescent samples are illustrated in Chapter 5.

e) Chapter 6 reports on the main conclusions and discusses some future perspectives of this research.

2 Properties and Fabrication Technologies of Random and Nanofiber Lasers

In this Chapter the properties of random lasers and their applications will be presented, together with an overview of the technologies used for the fabrication of NFs and more complex structures. In Section 2.1, NFs lasing mechanisms will be illustrated with a focus on random lasing. In Section 2.2, 3D printing and electrospinning technologies will be described. Section 2.3 will focus on systems that combine 3D printing and electrospinning techniques.

2.1 Random Lasing: Properties and Applications

Nanofibers made of organic light-emitting materials are advantageous for the realization of miniaturized lasers because of their elongated, almost 1D, shape, which favours light transport and amplification along the length of the fiber [7]. Moreover, the optical properties of NFs can be engineered by a proper combination of organic and plastic materials, for instance by doping transparent thermoplastic polymer matrices with low-molar-mass chromophores, inorganic quantum dots and nanowires. This Section will initially present various NFs lasing mechanisms so far investigated. After a brief introduction on the various architectures developed on the base of standard laser cavities, random and network lasers will be discussed.

2.1.1 Nanofiber Lasers

In a laser system, the optical cavity is an essential part because it provides the optical feedback that allows multiple passages of light through the active medium. In this way, the intensity of light with wavelength λ_L, matching the resonator conditions, is amplified through stimulated emission. For a traveling-wave amplifier the intensity signal (I) depends exponentially on the length (L) traveled by photons in the cavity embedding the active material according to the relation: $I = I_0\exp[L \text{ x } (g \text{ - } a)]$ [7]. In this expression, g is the gain coefficient of the active material and a is the loss coefficient. The lasing threshold is reached when the total gain in the cavity exceeds

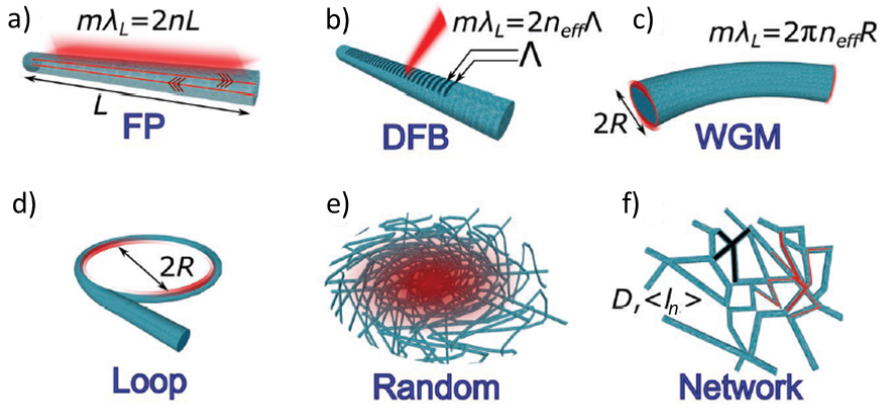

Figure 2.1: Optical cavities supported by NFs: a) FP resonator; b) DFB resonator, Λ is grating period; c) WGM microcavity; d) loop microcavity; e) random structures and f) network architecture. D is the number of connections of each node, $<l_n>$ is the average length of an edge of the network. Reproduced with permission from [7]. Copyright, 2019, Wiley-VCH Verlag GmbH & Co. KGaA.

the losses.

In the framework of nanophotonics, NFs are particularly interesting because for most of these organic structures both the resonator and the active material can be integrated in a single element [7]. Examples of NF lasing devices studied in the recent years include structures that reproduce Fabry Pérot (FP) resonators, whispering gallery mode (WGM) resonators and distributed feedback (DFB) gratings (figure 4.16).

The FP configuration (figure 4.16a) is based on highly reflective surfaces that enclose the active material. Simultaneous longitudinal modes are generally allowed in such cavities, following the equation $\frac{2nL}{\lambda_L} = m$, where n is the refractive index of the active layer and m is an integer number.

DFB is a type of laser based on periodic diffractive grating coupled with a thin gain material (figure 4.16b). In such structures, light is reflected at each interface between two adjacent media of the corrugated medium. The reflected rays constructively interfere at a certain wavelength, a condition that can be adjusted by choosing the material thickness and the periodicity of the grating.

WGM resonators (figure 4.16c,d) are circular structures with radius R, in which total reflection of light occurs on the inner surface. The resonant modes allowed by such

cavities are determined by the condition: $m\lambda_L$=$2\pi n_{eff}R$, where n_{eff} is the effective refractive index and m is an integer. NFs can also form closed loops (figure 4.16d), which can be also exploited as microcavities for light amplification and lasing.
There are also more complex structures, which have been recently developed, such as random and network lasers (figure 4.16e,f) which will be discussed in the following.

2.1.2 Random Lasers

Conventional lasers are designed to suppress multimode emission and their cavity is designed to select a well-defined emission wavelength. Instead, random lasers (in which light amplification occurs through light diffusion in a disordered medium with optical gain) benefit from a complex multimode emission [18]. Random lasers can be divided into two main families depending on the relationship between the system size, L, the light transport mean free path, l_n, and the light wavelength (λ). If $l_n < \lambda < L$, a strong scattering is present and the mode linewidth is less than the mode spacing, resulting in multiple peak emission. In the second regime, $\lambda < l_n < L$ and weaker scattering occurs. Here optical modes can overlap spectrally and spatially. This leads to the formation of extended optical modes that covers the entire system [18].
In arrays of NFs, the light emitted by the active materials can be guided and amplified through the single NF and disordered sheets arrays can be easily realized as the one schematized in (figure 4.16e). For these reasons, NFs are very promising for the realization of random lasers. In NFs systems, light diffusion and light amplification properties can be designed by the morphology of the individual fibers and by the architecture of the arrays made of them [7]. In order to achieve random lasing emission, NFs have to be doped with nanomaterials that provide optical gain [7]. For lasing to be possible, the typical thickness of the NFs slabs should be $\simeq 100$ μm [7]. In addition to this parameter, the spatial assembly of the NFs within the mat also affects lasing process. For example aligned or random NFs might have different lasing emission in terms of direction and polarization [7], and the exploitation of uniaxially aligned NFs allows the lasing thresholds to be lowered [19]. In [20] gold nanoparticle were used to achieve plasmon enhanced random lasing. In this sys-

tems, the lasing threshold can be controlled through the size of the embedded metal nanoparticle.

2.1.3 Network Lasers

Nanophotonic network lasers consist of interconnected miniaturized optical waveguides (figure 4.16f) [8]. Compared to a conventional nanophotonic structure (such as integrated photonic circuits or nanophotonic lasers), in nanophotonic networks complex and multiple interference of the light propagating through the network occurs, leading to the formation of different modes depending on the topology of the network [8, 21]. In addition, nanophotonic networks allows for separating the control of scattering (which occurs at nodes) and light transport and amplification. The former can be managed by the network degree, D, defined as the number of connections of each nodes (this definition exclude the nodes in the periphery), the latter by the average length of the edges, $<l_n>$, and the size of the network. Nanophotonic network lasers have been realized by using interconnected polymer NFs [8]. Figure 2.2a,b shows that by increasing the intensity of the pumping beam, bright spots appear in the fluorescence maps and emission with lasing properties occurs (figure 2.2c,d). Network lasers are characterized by multimode emission whose spatial profile can be studied by using a graph approach as shown in figure 2.2e, which illustrates examples of optical modes of the network either extended over the whole area of the network or localized in the centre of the network. In addition, the lasing threshold decreases as the network degree, D, increases, as shown in figure 2.2f-h. Another important feature of network lasing is the sensitivity to local perturbations that is illustrated in figure 2.2i,j, where different emission spectra are obtained by varying the spatial shape of the pumping beam.

2.1.4 Applications of Random Lasers

Compared to other laser sources, random lasers can be designed to have low spatial coherence while maintaining high brightness (Fig 2.3). This makes them useful for application in full-field speckle-free imaging. When a coherent light source is used in

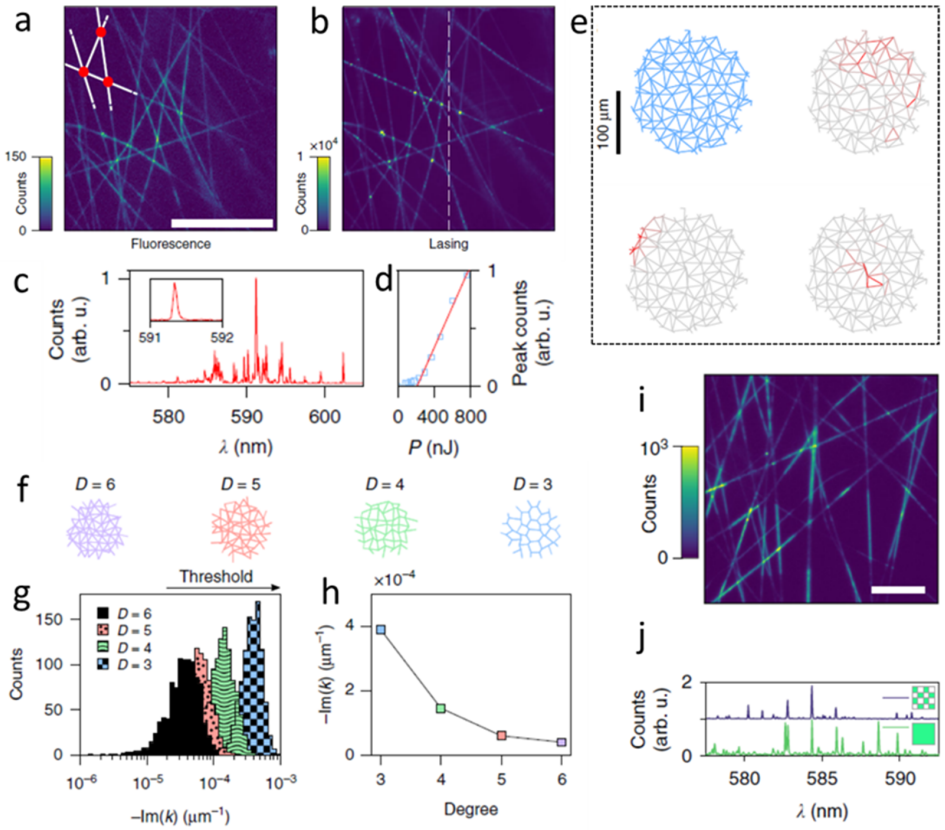

Figure 2.2: A network laser by organic NFs. a) Network edges (white lines) and network nodes (red dots). b) Bright spots corresponding to the network nodes. c) Lasing spectrum. d) Dependence of the emission intensity on the excitation energy. e) A network with 143 nodes and 293 edges, used for computing the lasing modes. f) Networks with diverse average degree, D. The corresponding excitation threshold distributions and lowest thresholds computed in an ensemble of 1000 different samples are shown in panels (g) and (h) respectively. Im(k) is the gain required for a mode with complex wavevector, k, to lase. i) Fluorescence map from a network of NFs optically pumped with a checkerboard pattern. Scale bar: 100 μm. j) Lasing spectra of (i). Reproduced with permission from [8] under the terms of the CC-BY license. Copyright 2019, The Authors, published by Springer Nature.

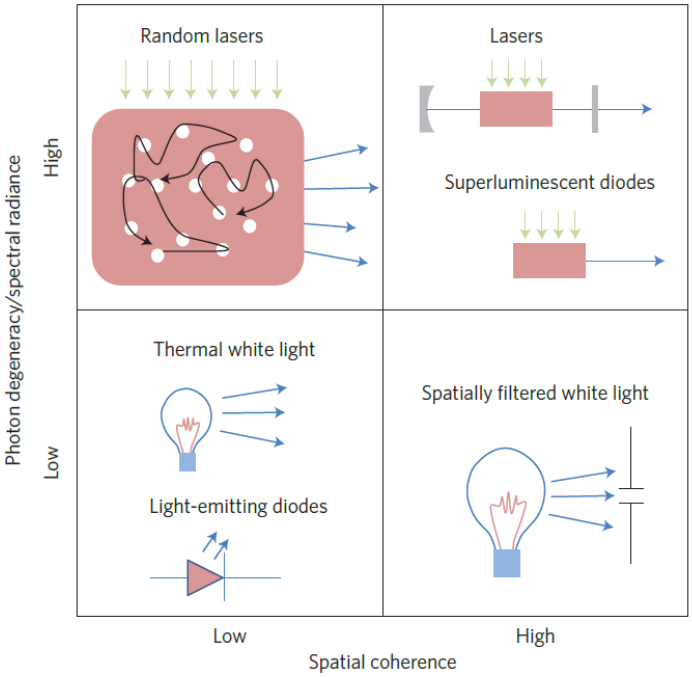

Figure 2.3: Different light sources compared in terms of photon degeneracy/spectral radiance and spatial coherence. Random laser presents low spatial coherence and high photon degeneracy/spectral radiance: the ideal combination for full-field imaging. Reproduced with permission from [6]. Copyright, 2012, Macmillan Publishers.

imaging, artifacts are formed due to interference occurring during image formation, such as the speckle [6]. The presence of speckle compromises the interpretation of the image by the observer. Figure 2.4 shows a 1951 US Air Force (AF) resolution test chart imaged with five different light sources with the setup schematized in figure 2.4a, evidencing that the exploitation of a random laser with low spatial coherence can prevent the formation of the speckle and allow superior quality images to be obtained, similar to that obtained with spatially incoherent sources [6].

Furthermore, in [5] a technique of super-resolution spectroscopy was reported based on a random laser source. The random laser has an emission spectrum with many sharp peaks. Their frequencies are uncorrelated and, because of this, the spectral response of a sample can be probed stochastically if such an illumination source is exploited. This allows the optical properties of the probed sample to be investigated with a spectral resolution higher than standard spectrometers.

Lasers based on polymer NFs have many features that make them useful for the

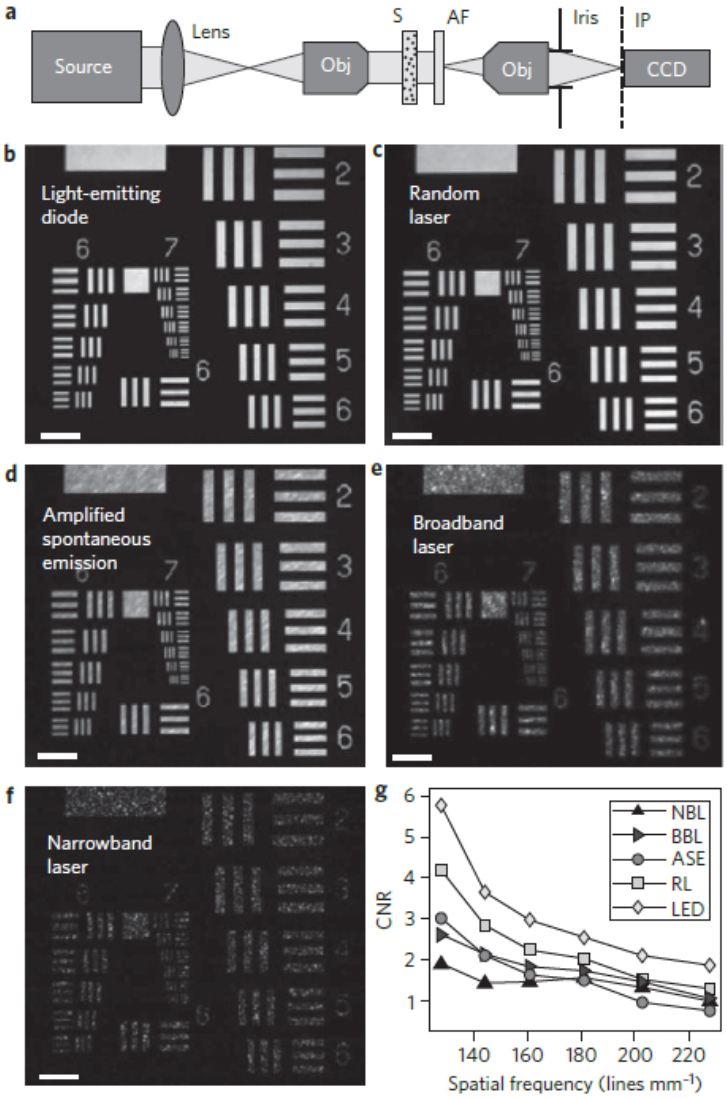

Figure 2.4: Five different light sources are used to image an Air Force resolution test chart. a) Schematic of the experimental setup. A scattering film was placed in front of the object, that resulted in speckled illumination of the object if the source was spatially coherent. The five sources used are: b) light-emitted diode, c) random laser, d) amplified spontaneous emission, e) broadband laser, f) narrow band laser. Scales bar 50 μm. g) Contrast-to-noise ratio (CNR) as a function of the spatial frequency of the features on the test chart. Reproduced with permission from [6]. Copyright, 2012, Macmillan Publishers.

applications described above, as well as for other fields. Some of the features are, for example, flexibility of active materials, biocompatibility, the capability to tune optical and mechanical properties and the possibility of realizing different types of resonator [7]. Lasers based on NFs can also be exploited for optical sensing applications. For example in [22], the variation of the refractive index of liquids has been investigated through the shift of lasing modes.

Motivated by the various potential applications, several methods have been developed for the realization of NFs and laser devices based on them, such as self-assembly from solution [23], soft lithographies technologies such as nanofluidic and nanoimprinting methods [24]. Recently also 3D printing technologies have been exploited for the realization of random lasers [25]. For the realization of NFs, ES is a versatile technique and allows macroscopic volumes of NFs to be produced [7]. The ES process exploits the electric field between a metallic needle and a collector, to extrude a viscoelastic polymeric solution [9]. In this work, ES and 3D printing technologies have been implemented and integrated in a unique system for the development of random lasers. In the following Section some additive manufacturing technologies will be presented, with a focus on the technologies used in this work. Afterwards, the ES process will be introduced.

2.2 3D Printing and Electrospinnig Technologies

Additive manufacturing, or three-dimensional printing (3DP), is the technology of building 3D objects layer-by-layer starting from a digital model of the object (computer aided design, CAD). The first example of this technology was stereolithography invented by C. Hull in 1986 [26]. Since then, there has been a great progress of this field, enabling the fabrication of devices with geometries previously unachievable, as well as with improved efficiencies and performance [27]. The typical 3DP process is based on the following steps: first, a CAD model of the object is realized, then the digital design is sliced into a predefined number of layers through dedicated software and, finally, the object is realized by printing the layers sequentially.

The first part of this Section will discuss the main 3D printing technologies, with a focus on the technique of Direct Ink Writing (DIW) and FDM used in this work.

The second part of this Section will present the electrospinning process.

2.2.1 Stereolithography

Stereolithography (SLA) is a process based on the interaction between UV light and a photosensitive liquid resin [28]. UV light is exploited to polymerize in a controlled way the resin. In a typical process, the build platform is positioned in order to define a thin layer of UV-sensitive resin. The UV beam used for photopolymerization is spatially structured in order to reproduce the predefined 2D pattern of each layers. After polymerization of an individual layer, the build platform is moved in a controlled way in order to realize the next layer. Based on the light projection techniques, SLA can be classified as (i) free-surface (top-down) printing and (ii) constrained-surface (bottom-up) printing. In the bottom-up approach, only one layer of resin is exposed to the UV beam, which illuminates the resin from the top side. After curing, the building plate moves down and a new layer of uncured resin is dispensed by a roller. [29]
In the top-down approach the building plate is dipped into a vat containing the resin, and UV illumination occurs from the bottom side. Each layer is realized by shifting vertically (i.e. by moving up) the building plate [29].
The factors that determine the effectiveness of the light curing process are the concentration of photoinitiators, their absorption properties, the intensity of the UV light and the exposure time [26].
The choice of the UV-sensitive resin depends on the specific application. To obtain an object with high optical transparency, acrylate-based resins are generally used. Acrylate-based resins have a refractive indices in the range 1.32-1.48 [30]. However, these materials have some limitations in terms of mechanical properties and poor biocompatibility. Although glass cannot be used in SLA, it is the preferred material for most applications in optics [26]. An approach for processing fused silica glass has been introduced recently which is based on the use of a nanocomposite pre-polymer with amorphous silica nanoparticles dispersed in a UV resin [31]. In this process the nanocomposite resin is structured through SLA and the fused silica glass object is obtained after a two post-printing thermal treatments. This approach produces

samples whose optical properties are comparable to that of other commercial glasses. SLA can achieve a spatial resolution of $\simeq$ 10-100 μm, which is higher than other additive manufacturing techniques. One of the main limitations of SLA technologies is the printing speed, which is determined by the curing rate of the resins. [26].

2.2.2 3D Printing by Extrusion

The limitations of stereolithography in terms of the need of photocurable materials are overcome by 3DP technologies based on material extrusion. In these techniques either an ink or a fused polymer filament is extruded through a nozzle with the help of temperature or pneumatic pressure. This Section will focus on the 3D printing technologies used in this thesis: DIW and FDM.

2.2.3 Direct Ink Writing

In DIW, the ink is inserted into a syringe that is connected to a needle and mounted in a 3D translation stage. The extrusion of ink through the needle is controlled by an applied pressure, and the 3D translation stage moves the nozzle in order to realize the pattern defined by the digital model in a layer-by-layer manner. Following the deposition, the ink solidifies rapidly by processes such as evaporation of the solvent, phase change and gelation [26]. DIW works at room temperature and without the addition of aggressive chemicals. Many variables must be taken into account for proper execution of DIW, some concerning the properties of the ink such as *viscoelasticity* and the *shear thinning* [32].

The rheological properties of the ink are determined by the used solvents, additive materials and binders. Selected materials are mechanically mixed for obtaining a printable ink. For example, to obtain a two gap structure, solid particles are added to the ink, in order to find a compromise between high stiffness and moderate shear yield [33]. The methods used for blending the various ink components are bath/probe ultrasonication, magnetic stirring, shear mixing.

In addition to the properties of the material used, it is important to understand how the printing parameters influence the thickness of the printed structures, which are typically deposited in a filament shape. In fact, by varying the process parameters

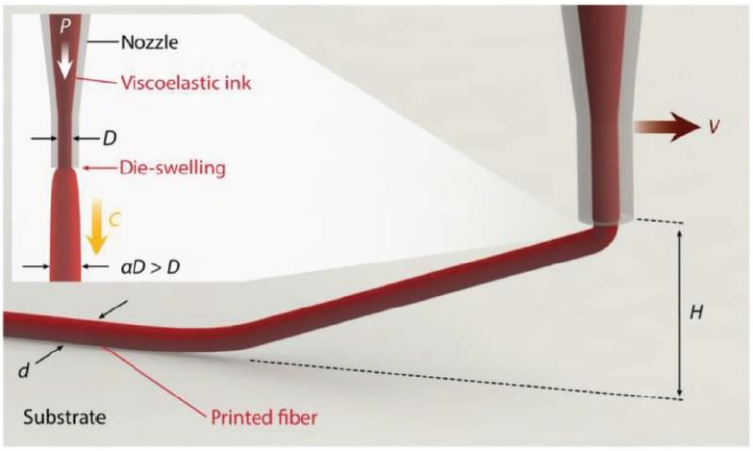

Figure 2.5: Schematic illustration of the main parameters of DIW 3D printing. Reproduced with permission from [34]. Copyright 2018, Wiley-VCH Verlag GmbH & Co. KGaA.

the shape fidelity and complexity of the printed sample can be changed [34]. A model reporting the dependence of the diameter of the printed filament, d, on the diameter of the nozzle (D) and the printing speed (C) has been proposed by Yuk et al. [34]. In this study the viscoelastic ink is extruded without deformation. The printing speed, C, is determined by the applied pressure, P, during 3D printing and the ink properties. By extruding a viscoelastic material, a die-swelling of the ink is usually obtained. This results in a filament diameter $d{=}\alpha D$, where $\alpha > 1$ is called die-swelling ratio (figure 2.5).

By referring to figure 2.5, where V indicates the moving speed of the nozzle and H the distance between the nozzle and the printing bed (or the substrate), and considering volume conservation, the extrusion rate can be derived [34]:

$$Q_1 = \pi C \frac{(\alpha D)^2}{4} \tag{2.1}$$

The authors of [34] derived a relation between the inner diameter of the nozzle and the diameter of the printed fiber d: $d{=}\alpha D\sqrt{\frac{C}{V}}$.

Indicating by V^* , H^* the adimensional parameters $V^*{=}\frac{V}{C}$ and $H^*{=}\frac{H}{\alpha D}$, respectively, the authors demonstrated that a single nozzle with simple straight motions can print fiber of different diameters and different patterns.

By varying H^* and V^* the study determined the intervals of values for which differ-

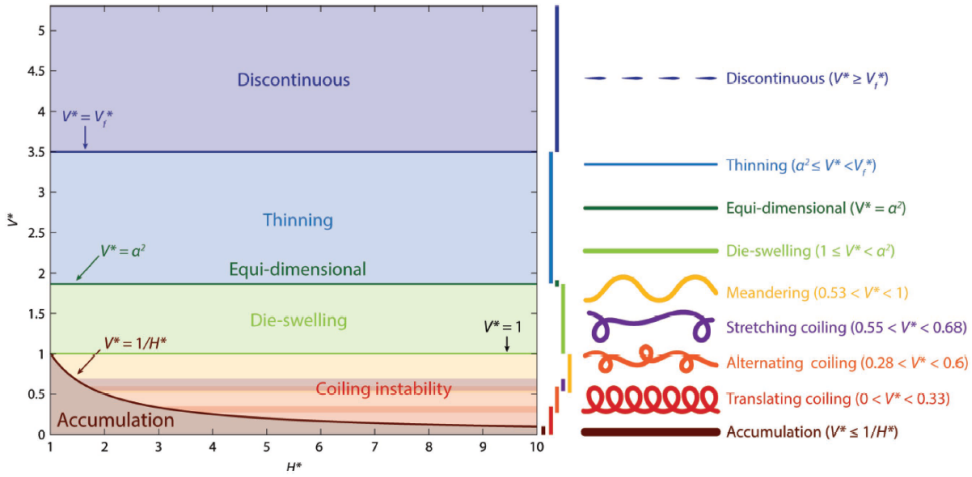

Figure 2.6: Phase diagram of the printing regimes explored by varying the two adimensionl parameters H^* and V^*. Reproduced with permission from [34]. Copyright 2018, Wiley-VCH Verlag GmbH & Co. KGaA.

ent filament features are obtained (figure 2.6), i.e. from continuous fiber of diameter much smaller than the nozzle diameter to non linear patterns as accumulation modes and coiling. More specifically, for H^*=1, various regimes were determined depending on the values of V^* :

$V* < 1$ is the condition for the accumulation mode, where the diameter of the printed fiber, d, can be much greater than the nozzle diameter D due to the amount of material deposited in the same point.

When V^* is greater than 1, various regimes can be achieved. The first is the case of die-swelling regime: the diameter of the printed fiber is larger than the inner diameter of the nozzle for $1 < V^* < \alpha^2$. The diameter of the printed fiber has the same value of the inner diameter of the nozzle when $V^*=\alpha^2$. By increasing the value of V^*, one enters in the thinning regime in which the diameter of the printed filament is significantly smaller than that of the needle. The range of the thinning mode is $\alpha^2 < V < V_f$, where V_f indicate the upper limit of the thinning mode, beyond which the printed filament begins to fracture.

When $H^*>1$, the printing regime are the same of those described before in the range $V^*>1$. For $V^* \leq \frac{1}{H^*}$, accumulation mode occurs while for $\frac{1}{H^*} < V^* < 1$ some coiling instabilities are present (figure 2.6).

The DIW has found several application in bioprinting, a technology which is currently being developed in order to build functional tissue constructs, with pre-programmed structure, that can replace damaged tissue. Structures realized by bioprinting can contain biomaterial and cells. The enormous development of extrusion bioprinting has led to the definition of two main sub-categories [35]:

- *Bioprinting of material scaffold for subsequent cell seeding*

  The scaffold should be made by cell-compatible materials and it is designed in order to mimic soft living tissue in terms of stiffness, porosity and mechanical behaviour [36]. The materials used for this approach are often made of biocompatible polymers such as PLA, polycaprolactone (PCL), and poly(lactic-co-glycolic acid) (PLGA) [37].

- *Bioinks capable of supporting direct deposition of embedded living biological matter*

  With the use of this type of ink, it is important that the deposition is gentle and does not impact the viability of the extruded cells [38, 39].

It is important to have a bio ink that allows a sample with the desired rheological, mechanical, chemical, and biological characteristics, as well as biodegradable and biocompatible [40]. The main limitation of materials used in DIW remains the mechanical properties, which limits the fidelity of the printed shape. To overcome these limitations, shear thinning materials are used, such that the weak interactions between biomacromolecule gels are disrupted during extrusion by the shear stress forcing the material to flow through a nozzle. When deposited on the platform, the molecules quickly regain their yield stress to balance the gravitational tension so that the molecules remain in the molded structure without collapsing [41].

2.2.4 Fused Deposition Modeling

FDM is a 3D printing technique in which a thermoplastic polymer is extruded through a heated head. The most used materials for FDM are polymethylmetacrylate (PMMA), polystyrene, polylactic-acid (PLA), acrylonitrile butadiene styrene (ABS), polycarbonate [26]. The filaments, typically with a diameter of 1.75 or 3 mm, are guided to the printhead by the mechanical movement of a spool and 3D deposition is accomplished by continuous movement of the nozzle [42]. The most common configuration is the Cartesian, in which the printing movement happens following the XYZ orthogonal axes [43]. The extrusion temperature depends on the melting characteristics of the material used (typical range of extrusion temperature is 200-400 °C). After extrusion, the filament solidifies when its temperature falls below the glass transition temperature of the polymer. The bed temperature (i.e. the temperature of the substrate used for building the 3D object) is an important parameter that can affect the correct deposition of the first layer and the adhesion between consecutive layers (typical range is 60-100 °C). The spatial resolution of the FDM technique is mainly determined by the size of the nozzle, and is typically of 100-400 μm.

In addition to the properties of the material used, a successful printing process depends on the correct combination of the bed temperature, the extrusion temperature, printing speed and the CAD parameters. This topic will be addressed in more detail in Chapter 3.

2.2.5 Electrospinning

In ES technique, NFs are fabricated using electrostatic fields to spin viscoelastic polymer solutions [9]. This technology has been studied extensively in the last ten years because it is capable of realizing NFs with diameters in the sub-micron range [44], and enables the fabrication of arrays of NFs with complex architecture. ES has great potential for applications, including filtration, nano-electronics [45], optical and chemical sensors, tissue engineering and biotechnology [45]. One of the most studied field is the realization of nanofibrous scaffolds for tissue engineering. In fact, one advantage of ES is its flexibility: it is capable of constructing continuous NFs from a very wide variety of materials. For tissue engineering materials such as collagen, cellulose, and other biopolymers are used as well as nano-composites, including ceramics [44].

Physical Mechanism:

In the typical ES setup (figure 2.7), a syringe is filled with a polymer solution that is pumped at a constant flow rate through the needle (spinneret). The solution is then extruded through the needle by applying a bias voltage between the needle and the collecting surface (collector), producing a polymer jet. During the time-of-flight between the needle and the collector the polymer jet is continuously stretched and the solvent evaporates, allowing for collecting solid state fibers with either micrometric or sub-micrometric diameters.

The needle-collector setup can be arranged both vertically or horizontally [9]. As long as the electrostatic force is less than the polymer solution surface tension, a polymer droplet is formed at the needle tip. The droplet formation is a key element of the process and, for it to be formed, the used polymeric solution must feature specific viscoelasticity and molecular entanglement properties [9]. When the electrostatic repulsion of the charges accumulated on the surface of the drop exceeds the viscoelasticity and surface tension of the solution, the apex of the droplet takes on a more elongated shape, the so called *Taylor cone*. For the surface tension to be overcome and the droplet to become a polymer jet, the applied voltage between the needle and the collector must be increased. The threshold value of the electric field F_t, for which the droplet is de-stabilized and the polymer jet is formed can be calcu-

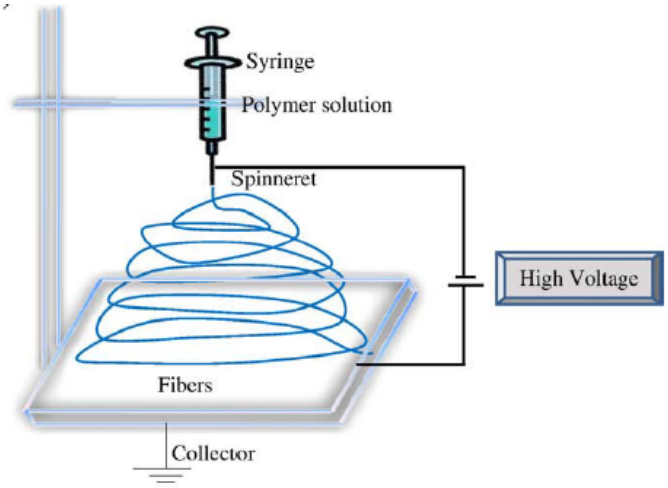

Figure 2.7: A typical electrospinning setup. Reproduced with permission from [44]. Copyright 2010, Elsevier Inc.

lated by equaling the electrostatic pressure and the Laplace pressure on the surface of the droplet [9]. The electrostatic pressure is $\frac{\epsilon_0 F^2}{2}$ and the Laplace pressure is $\frac{2\sigma_s}{R_t}$, where R_t is the radius at the apex of the Taylor cone, ϵ_0 is the dielectric constant, σ_s is the surface tension and F is the electric field calculated on the charged spherical surface. Therefore, the threshold value of the electric field is:

$$F_t = \sqrt{\frac{4\sigma_s}{\epsilon_0 R_t}} \tag{2.2}$$

The bias voltage for which the polymer jet is formed is typically of the order of 10^4 V. The polymer jet propagates from the needle to the collector, a path in which the solvent evaporates and individual nanofibers can thus be deposited on the collector as solid, continuous filaments either in ordered patterns or in disordered networks. The electrically charged jet is stable in the first part of the trajectory while during the flight it generally undergoes several different instabilities such as bending or wipping (figure 2.8). In such regime with the presence of instabilities, the diameter of the nanofibers reaches the lowest values, eventually forming fibers with sub-μm diameters [9].

Process Parameters:

Electrospinning is a complex process that involves different experimental variables. Predicting either the physical behavior of the polymer jet or specific geometry of

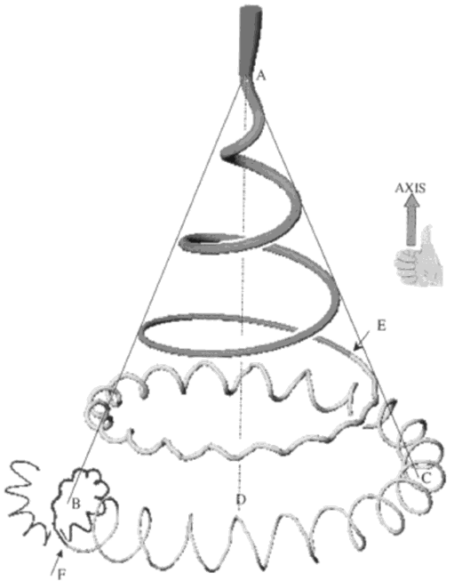

Figure 2.8: Typical trajectory of the electrospun jet. Instabilities to which it may be subjected during flight are depicted. Reproduced with permission from [46]. Copyright, 2006, American Chemical Society.

the electrospun fibers is a difficult task. In fact, many physical phenomena come into play simultaneously in ES such as viscoelasticity, capillarity and the solvent evaporation. Some of the parameters involved can be determined directly by the user (*primary*), while others depend on the characteristics of the polymer solution (*secondary*) [9]. However, it is possible to classify the process parameters into macrogroups:

- *Properties of the solution.* This group includes both primary parameters such as molecular weight and polymer concentration, and secondary parameters such as, for example, viscosity, which depends on the concentration and temperature at which the process takes place.

- *Setup variables.* This group includes basic parameters for the ES process, most of which are determined directly by the user, such as: the applied voltage, the flow rate, the distance between the needle and the collector and the needle diameter.

- *Ambient conditions.* These parameters include the humidity of the environment, which greatly influences the success of the process, the presence of spe-

cific gases in the atmosphere of the ES system, the ambient temperature.

2.3 3D Printing Combined with Electrospinning

There is a growing interest in additive manufacturing towards the combination of 3DP technologies and the ES. This approach allows for the production of architectures with multiscale complexity, high strength and new mechanical properties [47]. FDM is the most common 3DP technology to be combined with ES. Typically, the combination of the two technologies is achieved by using two separate and independent equipment for 3DP and ES. In such approaches, once the sample is printed, it is physically moved to the dedicated ES system.

T. Kozior et al. [47] combined two different 3D printing technologies (fused filament fabrication, photo-curing of liquid polymer resins) with ES. In particular, the scope of their work was a comparative analysis of how the fiber assembly and size were affected by the geometry and the materials used for 3DP. For 3DP processes the Makerbot Replicator printer (figure 2.9a) and a Connex 350 printer were used (figure 2.9b). Once the sample was printed, it was vertically attached on the collector of an ES system (Spinbox, Bioinicia) and NFs were electrospun on top of the printed structures (figure 2.9c). Samples produced by the above approach (figure 2.9d,e) were extensively studied and show properties suitable for filtration and medical applications.

In a different work [48], 3DP FDM (using a Fortus 400MC 3D printer) and ES (using TIC 1092012 machine, ATH, Bielsko-Biała) were exploited in order to realize a multifunctional layered scaffold for nasal cartilage implant (figure 2.10) .

Combination of solvent-cast direct-writing (SC-DW) and ES was reported in [12], with the purpose of realizing bioresorbable stents for cardiovascular applications. In particular, two methods of drug loading were compared: in the first, the drug was encapsulated in the printing ink (figure 2.11a); in the second one the drug was encapsulated in an electrospun poly(l-lactic-co-ϵ-caprolactone) membrane, deposited on 3D printed stents (figure 2.11b). With the second method, the release of drugs from the stents matches the dose and time required for *in vivo* applications. To realize tubular structures, a 3 mm diameter rotating spindle was placed in the 3D

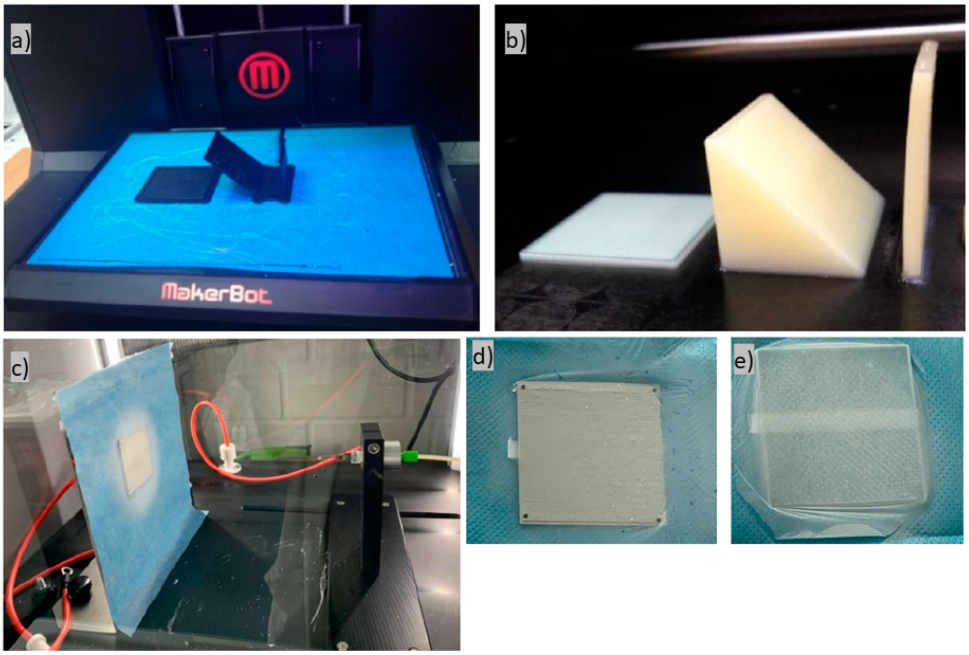

Figure 2.9: a) 3D samples prepared with FDM technology. b) 3D samples prepared with PJM technology. c) The 3D printed sample was moved to the dedicated ES system and a nanofibers mat was deposited on it. d) FDM sample coated with PAN nanofibers mat. e) PJM sample coated whit PAN/gelatin nanofibers mat. Reproduced with permission from [47] under the terms of the CC-BY license. Copyright 2022, The Authors. Licensee MDPI, Basel, Switzerland.

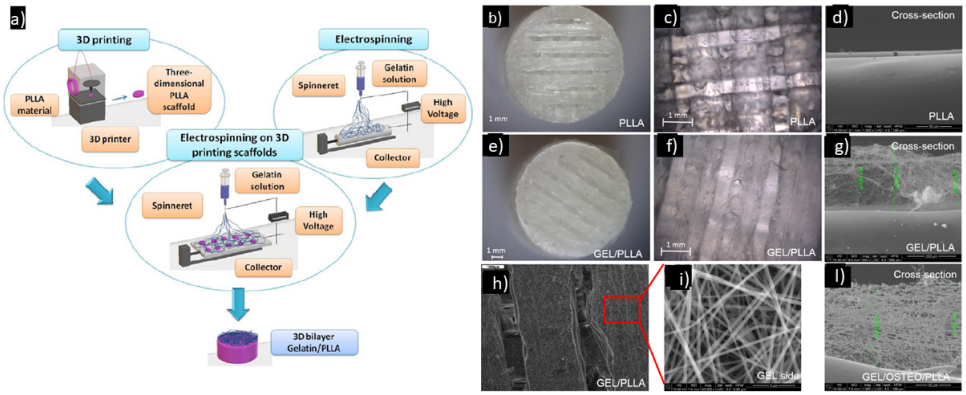

Figure 2.10: a) Process schematization. (b-d) PLLA scaffold. (e-i) Hybrid PLLA/GEL scaffold. l) Cross-section of hybrid scaffold. Reproduced with permission from [48]. Copyright 2018, Elsevier Ltd.

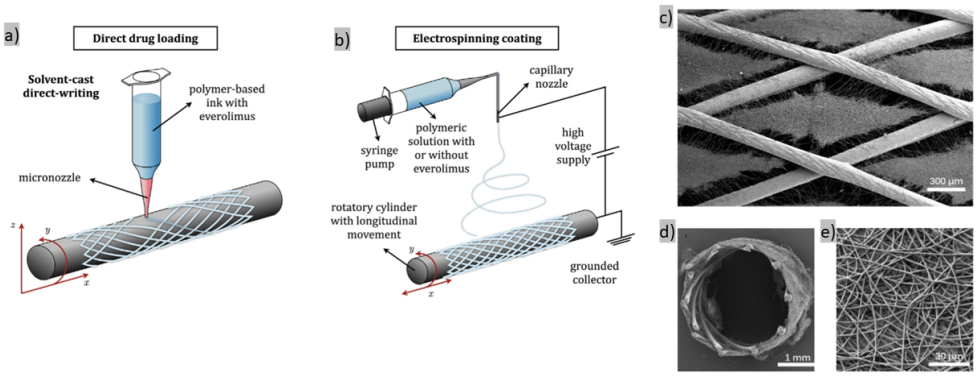

Figure 2.11: a) Printing setup for drug-loaded stents, where the drug is dissolved in the polymeric ink. b) Combination of SC-DW and ES to obtain fiber-coated polymer stent. c) Images of samples of the stents with initial NFs coating, evidencing polymer fibers deposited onto the metallic collector in between stent structures. d) Stent cross-section. e) Images of electrospun fibers, with diameter in the range of the micrometers. Reproduced with permission from [12]. Copyright 2023 The Author(s). Published by Elsevier B.V.

printer. Once printed, the stents were mounted onto a grounded collector mandrel capable of both rotation and translation. Here the stents were coated with the ES fibers (figure 2.11c-e).

Recent research efforts are being devoted to the design and realization of fabrication equipment which integrate in a unique device both 3DP and ES. Such systems are largely desired because of the possibility to realize in a unique run and place hybrid samples, decreasing the possibilities of sample contamination and degradation. In the following, some examples of devices that combine together 3DP and ES technologies are presented. A review of recent advances in the field is reported in [49].

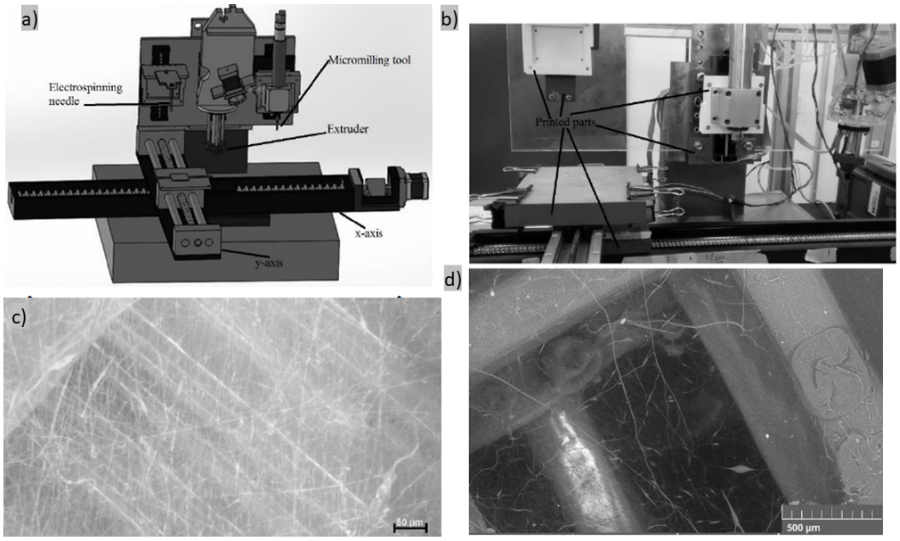

Figure 2.12: a) CAD design and b) photograph of the ES/printing system. c),d) Images of the hybrid scaffolds embedded with PCL fibers. Reproduced with permission from [50]. Copyright 2015, Society of Plastics Engineers, Published by Elsevier Ltd.

2.3.1 Examples of Systems Combining 3DP and ES

In ref. [50] a system was designed to allow for the fabrication of biodegradable hybrid 3D scaffolds using a combination of three different manufacturing techniques, namely FDM, ES, and micromilling. The combined system consists of two translation axes in XY plane and a vertical translation axis containing the printing tools: the ES spinneret, the FDM extruder and the micromilling tool (figure 2.12a,b).
The system was designed for the realization of 3D printed scaffolds with PCL nanofibers deposited between the object layers (figure 2.12c,d). In a typical process, some layers of the scaffold are printed by FDM. Afterwards the printing bed is moved along the X-axis towards the electrospinning spinneret. The temporal duration of the ES process must be predefined during the initial process setup, and may vary from one layer to the other. Once the ES process is finished, the printing bed is moved back and 3D printing is resumed. This process can be repeated many time as desired. To control the movement of the device axes and the duration of the ES process, a custom software interface was developed.
In another work [51], scaffolds were fabricated through a dedicated 3D bioprinting platform, which combined extrusion 3DP with multi-nozzle ES. The system consists

of a bio-printing head mounted on a three axis robotic system and an ES system used to realize NFs of biopolymers loaded with multiple drugs (figure 2.13a). The bio-printing head is connected to a computer for the control of process variables such as pressure, feeding speed and shape of the scaffold. For the bio-printing Gelatin, sodium alginate (SA) powders, and calcium chloride (CaCl2) were used.

In this study, two types of nanofibers were fabricated: PVA fibers were fabricated from a mixture made of 8.8% w/w PVA in deionized water and 1% w/w gentamycin sulfate (GS) in deionized water using a blend electrospinning process. Core–shell fibers were also fabricated (figure 2.13b-e).

Recently, some systems were reported in which 3DP and ES are combined in single fabrication platform, without the need of moving the printing plate between two separated 3DP and ES heads by means of linear translation stages. Faraz et al. [15] have developed a hybrid bioprinting-ES system for application in vascular tissue engineering. The system consists of three major sub-assemblies: one bioprinting head, two ES heads, which can be used for the co-electrospinning two different materials, and one needle collector assembled as shown in figure 2.14a,b. In this setup the bioprinting head can print tubular structures, around the rotating needle collector, similar to those found in the natural blood vessel. An Arduino Mega 2560 and a Ramps 1.4 3D printer controller board were used to manage the experimental variables of the hybrid bioprinting-electrospinning setup. A Smart Graphics LCD shield acts as an interface to the user, who initially have to choose one of the two available operation modes and then set the critical printing parameters. For the bioprinting mode the user can set the printing head position and the speed of the rotating needle. When ES mode is chosen, the bioprinting head is moved away from the needle collector, and the needle collector rotational speed has to be set by the user, who can interrupt, terminate, or resume the process at any time. The main limitation of this configuration is that it allows only tubular structures to be realized, as shown in 2.14c,l.

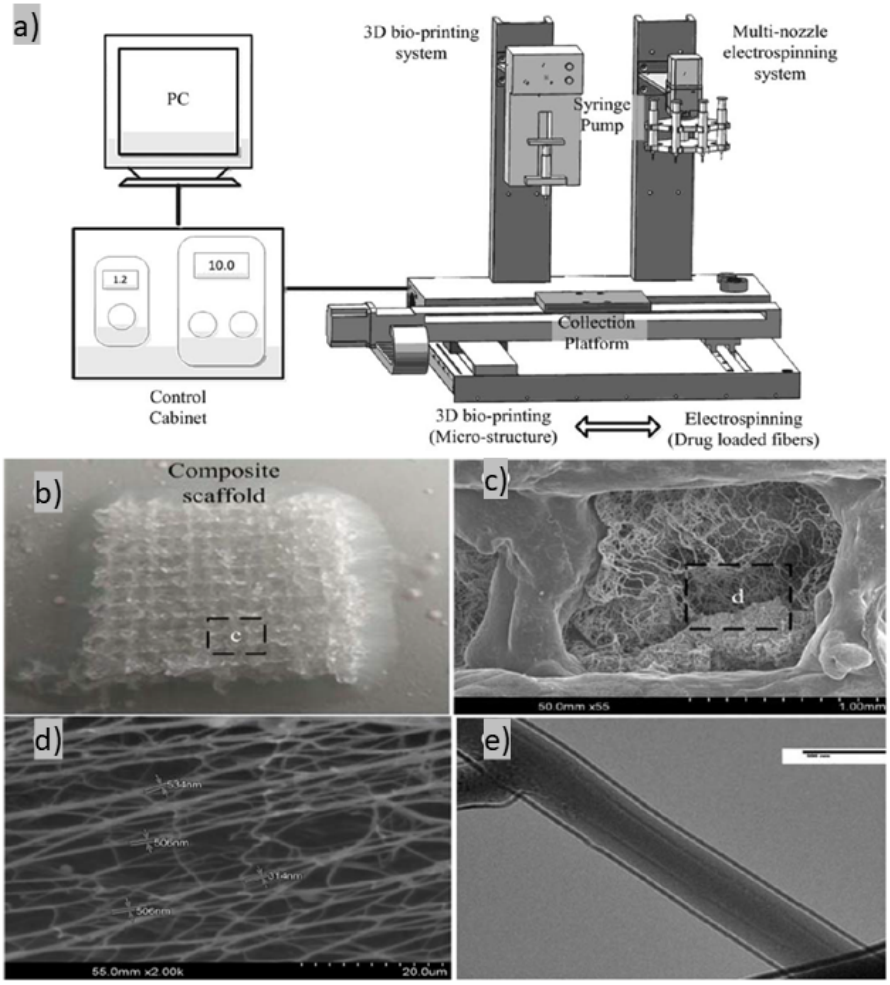

Figure 2.13: a) Scheme of the system combining 3D bio-printing and multi-nozzle electrospinning. b) Photograph of a composite scaffold with electrospun fibers. c) Scanning electron microscopy (SEM) micrograph of a composite scaffold. Scale bar: 1 mm. d) SEM micrograph of electrospun PVA nanofibers. Scale bar: 20 μm. e) Transmission electron microscopy image of PCL-PVA coaxial nanofibers. Scale bar: 500 nm. Reproduced with permission from [51]. Copyright 2015, Society of Plastics Engineers. Published online in Wiley Online Library.

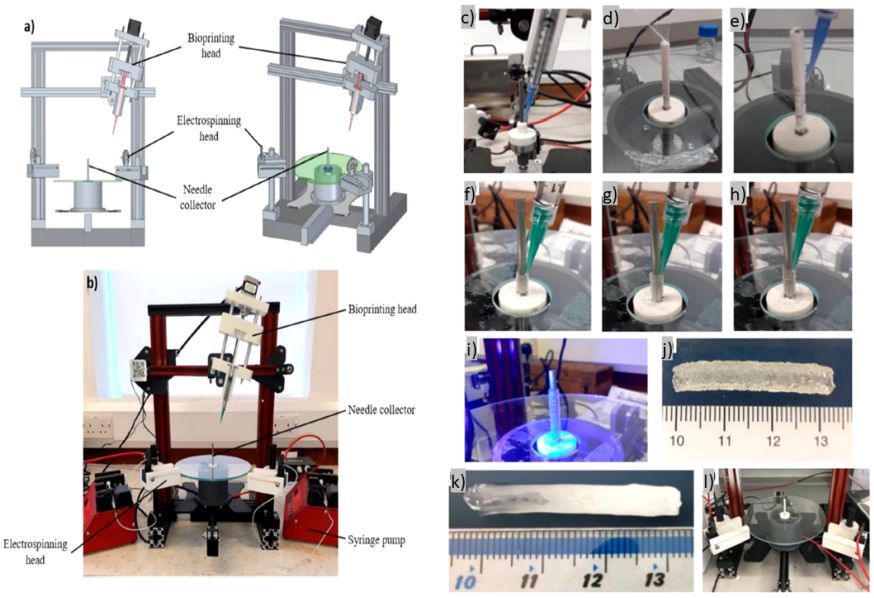

Figure 2.14: a) CAD model of the system. b) Photgraph of the device. c)-l) Photographs of various steps of the hybrid bio-printing and ES processes and of the resulting tubular structures. Reproduced with permission from [15]. Copyright 2021, IPEM. Published by Elsevier Ltds.

J. Dong et al. [52] have developed a hybrid system, which integrates thermal extrusion and ES techniques, in order to fabricate bone scaffolds. The aim of the work is to enhance the scaffold surface area with a layer of electrospun fibers. The setup is shown in figure 2.15a,b.

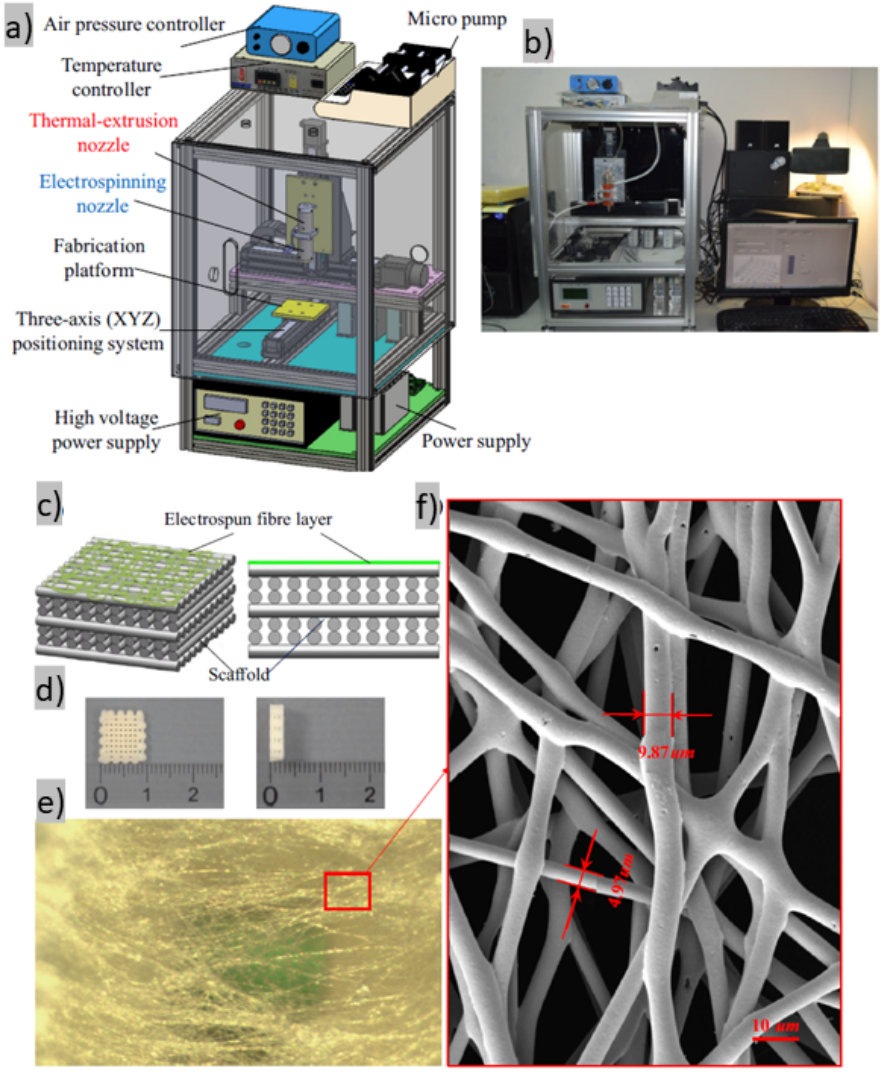

Figure 2.15: a) Schematic of the hybrid 3DP/ES system. b) Photograph of the developed hybrid fabrication system. c) Schematic representation of the hybrid scaffold. d) Photograph of printed scaffold. e) Optical image and f) SEM micrograph of electrospun fibres. Reproduced with permission from [52]. Copyright 2019, Springer-Verlag GmbH Germany, part of Springer Nature.

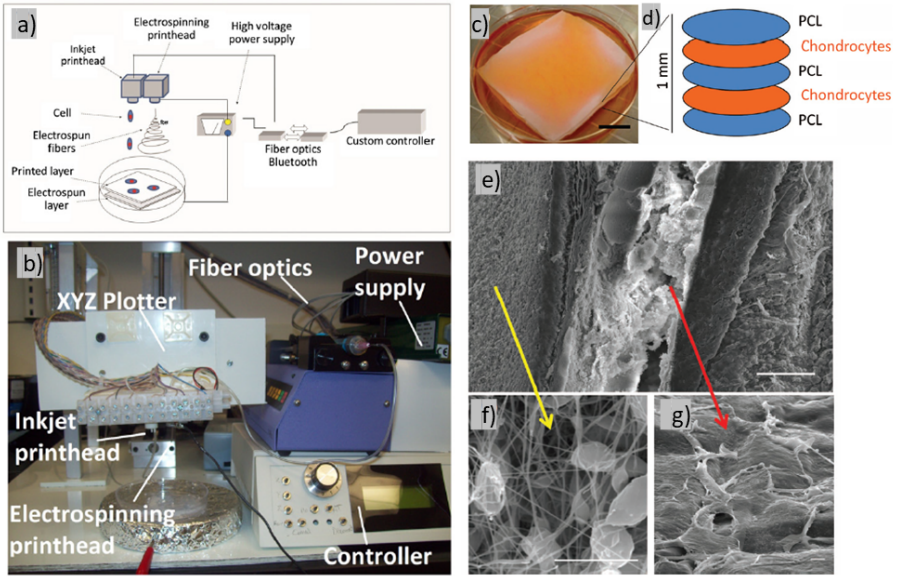

Figure 2.16: a) Schematic representation of the hybrid printing system based on the inkjet printhead and the electrospinning head. b) Photograph of the prototype of the hybrid printing system. c) Macroscopic image of the printed scaffols in a culture media. Scale bar: 2 cm. d) Schematic representation of a five-layer printed structure made of PCL and chondrocytes. e) Cross-sectional SEM micrograph of the layered scaffold. Scale bar: 100 μm. f)-g) Magnified SEM micrographs of the nanofibers and chondrocytes, respectively. Scale bars: 10 μm. Reproduced with permission from [53]. Copyright 2013, IOP Publishing Ltd.

T. Xu et al. [53] reported the realization of a hybrid inkjet printing/electrospinning system that can be used for cartilage tissue engineering applications. The proposed approach was based on the addition of an electrospinning system to an inkjet printing device (figure2.16a). Electrospinning was exploited for the realization of a layer of PCL NFs, whereas the inkjet system served for the deposition of a solution containing chondrocytes suspended in a fibrin–collagen hydrogel onto the electrospun PCL fibrous scaffold layer. The process of nanofibers and chondrocytes deposition was iterated several times and the final construct consists of five layer (three electrospun layers, two gel layers) and is shown in figure 2.16c-g. These structures formed cartilage-like tissues.

Most of the examples of systems combining ES and 3DP shown above were realized for biotechnological applications, whereas little has been done for photonic applications. In the following Chapters, the experimental results regarding the realization of a system combining FDM and ES techniques and the exploitation of such device

for the realization of NFs random lasers will be shown.

3 Materials and Methods

This Chapter will introduce the materials used for the realization of the electrospun NFs and the printed structures, and the experimental systems used in this work. In Section 3.1 the equipment for DIW will be presented, with a description of the materials used and the realized samples. In Section 3.2, the main properties of the materials employed for the realization of the samples through the combination of FDM and ES will be discussed. In Section 3.3 the apparatus realized in this thesis based on FDM and ES will be presented. Finally the methods for the characterization of the properties of the samples will be introduced.

3.1 DIW

3.1.1 Materials

Polydimethylsiloxane

Polydimethylsiloxane (PDMS) is a two-part polymer belonging to the group of silicone compounds. It is made of Silicon, Oxygen, Hydrogen and Carbon, and it is composed by a repeating monomer ($Si(CH_3)_2$ - O) and a flexible chain of Si-O as a backbone [54] (figure 3.1).

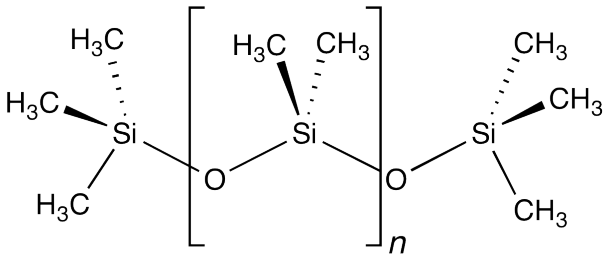

Figure 3.1: Molecular structure of PDMS.

Properties	**SYLGARD**^{TM}	**DOWSIL**^{TM}
Color	Colorless	White
Working Time @ 25 °C (Pot Life – hours)	1.5	8
Viscosity (Mixed) (Pa-sec)	3.5	542
Heat Cure Time @ 150 °C (minutes)	10	30
Tensile Strength (MPa)	6.7	6.8
Suggested mixing weight ratio (curing agent:base)	1:10	1:10

Table 3.1: Properties of the components of the ink used for DIW. Data for SYLGARD^{TM} are from [60], whereas data of DOWSIL^{TM} are from [61]

PDMS is easy to handle and manipulate, gas permeable, thermally stable, optically transparent, biocompatible and nontoxic [55]. The number of repeated units ($Si(CH_3)_2$ - O) determines the molecular weight and, consequently, the viscoelastic properties of the material. Moreover, the viscoelastic properties can be varied depending on the required application either by controlling the cross-linking of the polymer [56], or by adding fillers [57]. The versatility of PDMS makes it a material used for various applications, such as biomedical implants, lab-on-a-chip and microfluidic devices[58, 59] . In this work, two different type of PDMS were combined to achieve the required properties for DIW: SYLGARD^{TM} 184 Silicon Elastomer and DOWSIL^{TM} SE 1700 Clear W/C (table 3.1).

Ink Preparation

The ink for DIW was composed of 85% DOWSIL SE 1700 and 15% SYLGARD 184 (weight ratio). For both elastomers, the 1:10 weight ratio between the curing agent and the base was used. The properties of each component of the ink are summarized in table 3.1.

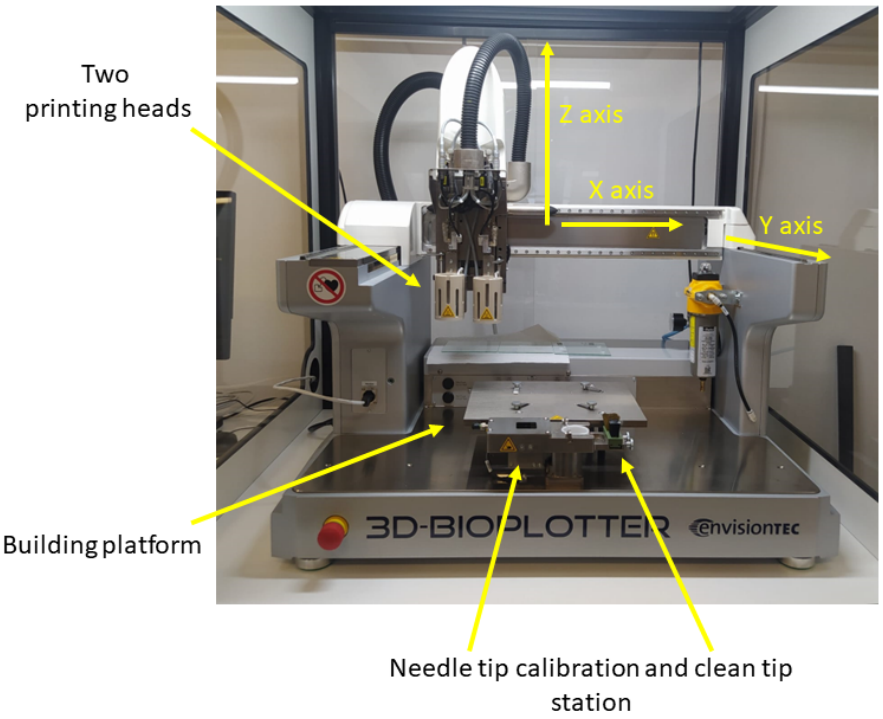

Figure 3.2: Photograph of the 3D-Bioplotter, EnvisionTEC, Starter series.

3.1.2 Bioplotter

The 3D Bioplotter Starter series, manufactured by EnvisionTEC (figure 3.2) was used for the DIW process. This system has two printheads, which allow for multi-ink printing by changing automatically the printhead during the process. The ink to be printed is fed into a cartridge, which is positioned in the printing head and connected to filtered compressed air through a hose. The cartridge is also equipped with a nozzle, generally of 0.2 or 0.4 mm of diameter. The printhead can operate at two different temperature regimes: (i) room temperature or (ii) high temperature. The high temperature mode is generally used for the extrusion of thermoplastic polymers, whereas the room temperature mode is generally used for viscous inks. In the latter mode, luer-lock needles and polypropylene cartridges are used, while reusable stainless steel cartridges and metallic needles are used for high temperature operation. The operational temperature mode can be selected individually for each printhead. The printhead movement in the X-Y direction is realized through linear

magnetic rails, while the spindle enables the Z-axis movement, with a resolution of X, Y, Z directions of 1 μm.
Before starting the printing process, the 3D CAD must be sliced. This can be done with a 3D CAD editing software, Perfactory RB by EnvisionTEC, that is available in the PC connected to the Bioplotter. The Perfactory RB software allows for setting:

- The shape of the printing substrate;
- The positioning of the object to be printed on the specific substrate;
- The scale and the orientation of the object to be printed;
- The thickness of each layer of the object;

The Bioplotter hardware is controlled through the Visual Machine software. Typically, the file of the sliced object, generated by Perfactory RB, is imported in Visual Machine, in which the following printing parameters can be set:

- Printing velocity;
- Extrusion pressure;
- Printhead temperature;
- Distance between needle tip and substrate;
- The printing pattern of the object to be printed.

Through the Visual Machine software, the user can select two initial processes to be done before starting the printing phase: the first is the automatic calibration of the needle tip position, which is made through the use of two light sensors with an accuracy of 0.03 mm. The second process is the automatic nozzle cleaning, which consists of extruding the material onto a dedicated Teflon base and passing the nozzle over either a metal or a plastic brush, depending on whether the nozzle is used for high temperature or room temperature operation, respectively. Such two initial processes are very important for the successful printing of the object.

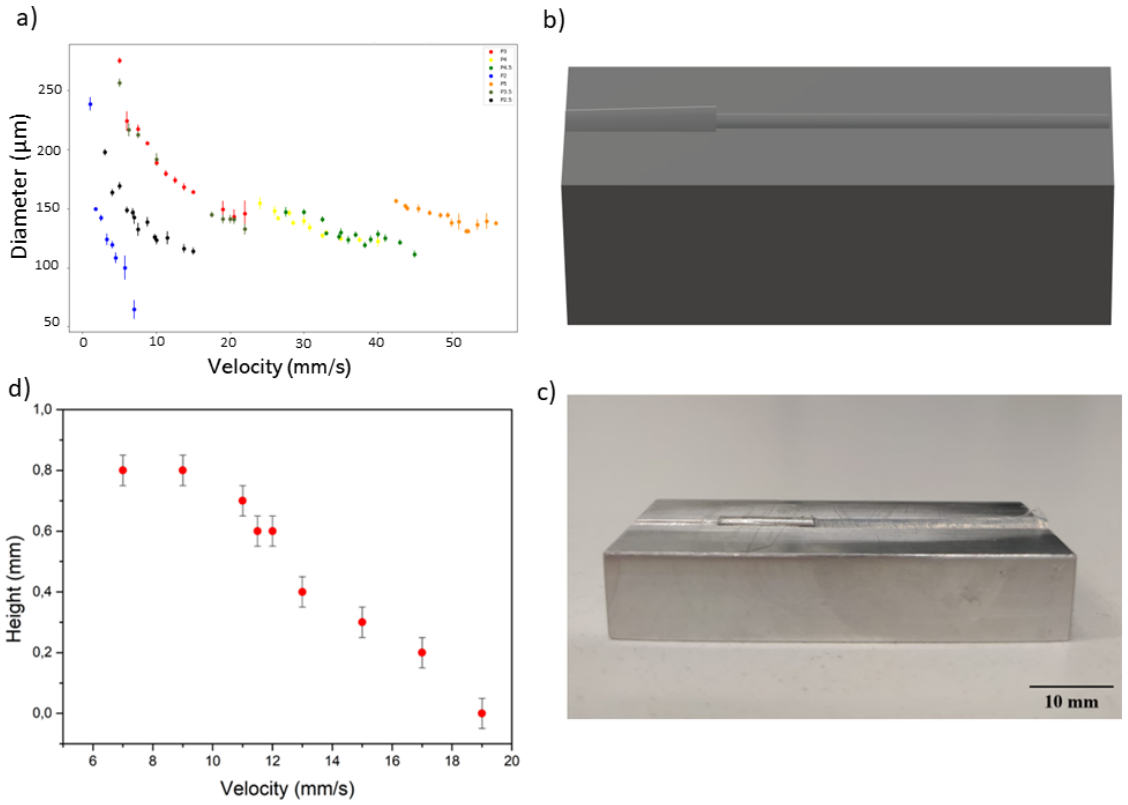

Figure 3.3: a) Filament diameter as a function of the printing velocity for different pressure values. b) Schematics of the structured substrate designed in order to print a waveguide coupled to the crystal. c) Photograph of the realized substrate with an Al cylinder with size comparable to the crystal and a PDMS printed filament. d) Height of the PDMS filament relative to the printing substrate as a function of printing velocity.

3.1.3 Results

The Bioplotter was used in order to realize polymer filaments and to explore the possibility of using 3D printed flexible filaments as waveguides coupled to a light-emitting Yb-doped $LiYF_4$ crystal [62]. To this aim, a preliminary analysis of the diameter of filaments printed on a glass substrate was carried out varying the printing parameters. The morphology of the printed filaments was investigated through an inverted microscope, and the diameters were derived by analyzing the optical microscope micrographs with "ImageJ." Figure 3.3a shows the values of filament diameters as a function of the printing velocity, V, for different printing pressures. A decrease of the diameter of the filament with increasing printing speed was found for each applied pressure as expected from the model of [34], in which the following

relationship was predicted (see also Chapter 2):

$$d = \alpha D \sqrt{\frac{C}{V}} \tag{3.1}$$

Since filaments printed on a flat substrate did not feature a fully cylindrical shape, a substrate was designed in order to template the filament during 3DP and have a more rounded final shape. In particular, the substrate (a parallelepiped with size 10 mm $\times$ 50 mm $\times$ 20 mm) has two adjacent channels, with semi-cylindrical shape, of different length (diameter about 2 mm, figure 3.3b,c):

- one with 20 mm length made to hold the crystal;
- one with 30 mm lenght made to hold the printed PDMS filament.

An optimization of the printing parameters was performed by using a prototype Al cylinder in place of the crystal, in order to not damage the fluorescent sample during the preliminary printing phases. The scope of such investigation was to obtain a PDMS filament with the same height as the crystal (as measured with respect to the template substrate). Figure 3.3d shows the values of the printed filament height obtained by varying the printing speed. These preliminary experimental investigations will be exploited for printing the waveguide nearby the crystal and investigate the coupling efficiency and waveguiding properties, using the light emitted by the crystal upon optical pumping.

3.2 Materials for FDM and ES

3.2.1 Vetroalfa

Vetroalfa (Filoalfa) is a polymer filament for FDM made by a transparent copolymer (butadiene-styrene). The main properties of Vetroalfa and the printing parameters suggested by the manufacturer are summarized in table 3.2.

Properties	**Value**
Diameter	(1.75 ± 0.05) mm
Density	1,01 g/cm3
Melt Flow Index	10 ml/10 min
Tensile strength	27 MPa
Flexural Modulus	1400 Gpa
Flexure Strength	36 Mpa
Heat Deflection Temperature	83 °C
Printer setting	**Suggested value**
Extruder Temperature	210-230 °C
Printing Speed	40-70 mm/s
Bed temperature	70-90 °C

Table 3.2: Properties of Vetroalfa from [63]

Color	Applegreen
Material	PLA
Features	Antibacterial
Printing technology	FDM
Filament diameter	2.85 mm
Nano-additive concentration	1%
Tensile Yield Strength (MPa)	60
Tensile Strength at Break (MPa)	53
Printer setting	**Suggested value**
Extruder temperature	190–210 °C
Printing Speed	40–50 mm/s
Bed temperature	0-60 °C

Table 3.3: Properties of PLACTIVE^{TM} from[65]

3.2.2 PLACTIVE^{TM}

PLACTIVE^{TM} (Copper 3D) is an innovative antibacterial nanocomposite material used for 3D printing medical devices. It is made of PLA and a Copper additive. Printed structures made of PLACTIVE^{TM} retained the antibacterial properties of the pristine filament after extrusion and were capable of eliminating various bacteria and microorganisms [64]. The main properties of PLACTIVE^{TM} are summarized in table 3.3.

Diameter	1.75 mm
Features	Electrically conductive
Polymer matrix	PLA
Volume Resistivity	0.78 Ωcm
Color	Black
Extruder temperature	220 °C

Table 3.4: Properties of the graphene/PLA filament. Data from [67]

3.2.3 Graphene Composite

A polymer graphene-based PLA filament (Graphene 3D Lab) was used for FDM printing. This composite filament allows for 3D printing electrically conductive components. This material has a volume resistivity of 0.78 Ωcm [66]. The properties of the graphene/PLA filament are summarized in table 3.4.

(a) Fully hydrolyzed (b) Partially hydrolyzed

Figure 3.4: Chemical structure of the two different types of PVA.

3.2.4 Polyvinyl-alcohol (PVA)

Two different PVA were used:

- Mw 13.000-23.000 g/mol, 87-89% hydrolyzed (Sigma Aldrich);
- Mw 85.000-124.000 g/mol, 99+% hydrolyzed (Sigma Aldrich)

Both PVA polymers were dissolved in distilled water, in order to obtain solution with different PVA/water w/w concentrations. PVA is produced on an industrial scale by hydrolysis (methanolysis) of the polyvinyl-acetate (PVAc), it is biodegradable and biocompatible [68].

Based on the conditions of idrolization, one can distinguish between fully hydrolyzed PVA and partially hydrolyzed PVA (figure 3.4a,b). For dissolution in water, the solution should be heated at a temperature generally >80 °C for the fully hydrolyzed PVA, while for the partially hydrolized PVA, the temperature for dissolution in water increases with increasing molecular weight [69].

3.2.5 Rhodamine B

Rhodamine B (Sigma Aldrich) was used in this work as a laser dye. RhB is a xanthene dye and has chemical formula: $C_{28}H_{31}ClN_2O3$. RhB is generally used as the active medium in pulsed and continuous wave dye lasers [70]. The RhB molecular structure is shown in figure 3.5.

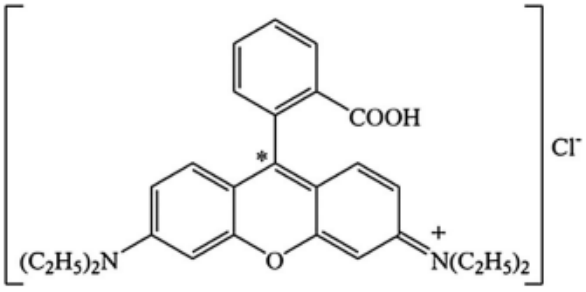

Figure 3.5: Molecular structure of RhB

3.3 Setup for FDM and ES

The system developed in this thesis combining 3DP and ES is based on FDM 3DP technology. A photograph of the realized system is shown in figure 3.7. The FDM and ES setups were placed in a dedicated movable table (figure 3.6) and enclosed in a plexiglass box, with a series of holes on the top and bottom layers. This configuration allows a continuous flow of air to be established through the fabrication volume by using a dedicated filtration column (mod. CHEMTRAP H402 Smart, Erlab). The plexiglass box has eight windows which provide access to all the areas of the system (figure 3.7).

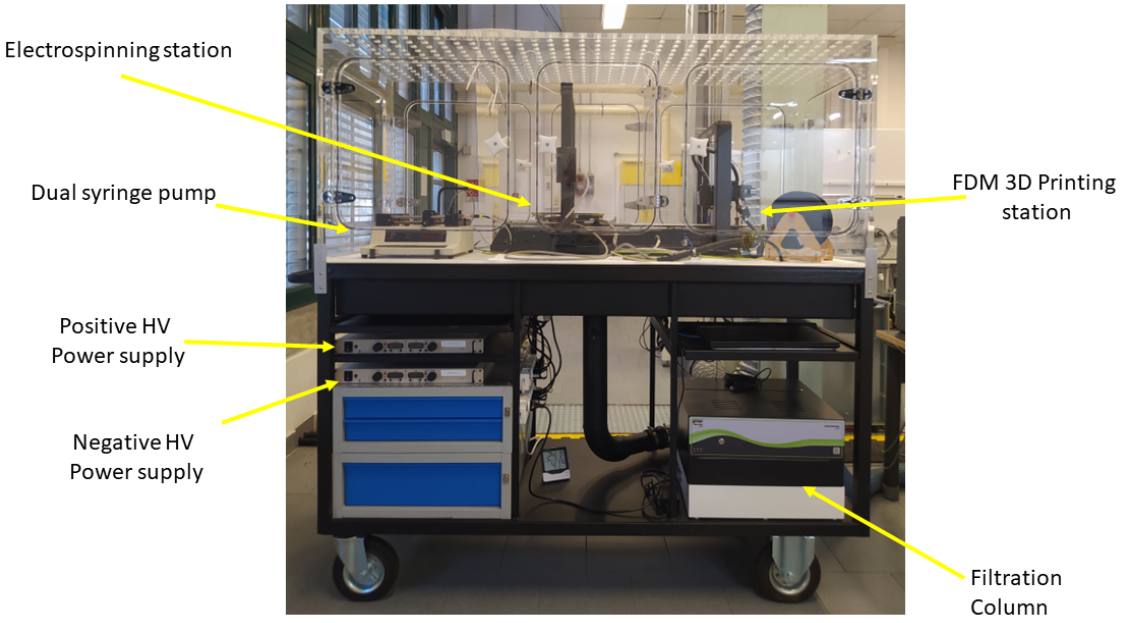

Figure 3.6: Photograph of the system combining 3DP and ES houses.

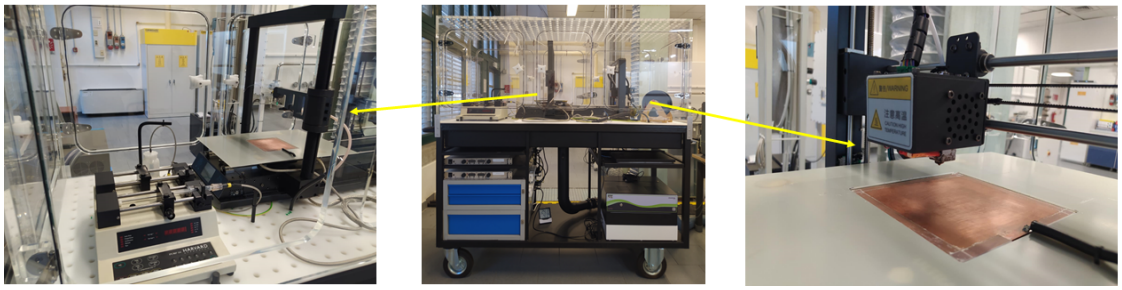

Figure 3.7: Photographs of the system combining FDM (right photograph) and ES (left photograph).

This Section will initially present the FDM setup and, successively, the ES system.

3.3.1 Fused Deposition Modeling 3D printer

The FDM printer is the Anycubic i3 mega whose metal frame was modified, by extending its length, adding a dedicated ES station and allowing the building plate to be moved between the FDM system and the ES one back and forward. The building plate of the FDM system is made of a Copper foils, which can be either grounded or negatively biased during the ES process. In addition, the temperature of the building plate (i.e. the bed temperature) can be varied experimentally from room

temperature up to 110 °C. Before operating the FDM system, a preliminary alignment of the building plate must be performed in order to place it perpendicularly to the vertical (Z) direction, along which the extruder is moved. This alignment is performed manually by the user, placing the nozzle almost in contact with the Copper building plate in 5 different positions, and by adjusting the dedicated four screws available at the four vertexes of the building plate.
Once the digital model of the object to be printed is available as a .STL file (that is a particular file format used for 3D digital models), such project must be imported in a software for the slicing process. To this aim, Ultimaker Cura software was used. In this step one can define the slicing properties, as well as other printing parameters. In particular, with Ultimaker Cura the following process parameters can be set:

- Bed temperature;
- Extruder temperature;
- Diameter of the printed filament;
- Layer thickness, that depends on the printed material and the extruder diameter. It is the height of each printed layer.
- Printing speed that is the speed with which the printing tip moves in the XY plane;
- Infill pattern, i.e. the pattern with which the inner volume of the printed objects are filled. The most common patterns are honeycomb, grid, triangles (3.8a-c) and parallel lines (figure 3.8d). For the pattern made of parallel lines, the angle formed by each line with respect to the X-axis (parameter "raster angle", figure 3.8d) of the printer can be varied. Moreover, the distance between the lines of the infill pattern can be also varied. This is the "Air gap" parameter (figure 3.8d). Finally the width of each line of the infill pattern can be also selected ("Raster width" in figure 3.8d);
- Infill density that is the fraction of the inner area of each layer that is filled with printed material. Example of varying infill density are shown in 3.8a-c, where from left to right increasing infill densities are displayed for each patterns.

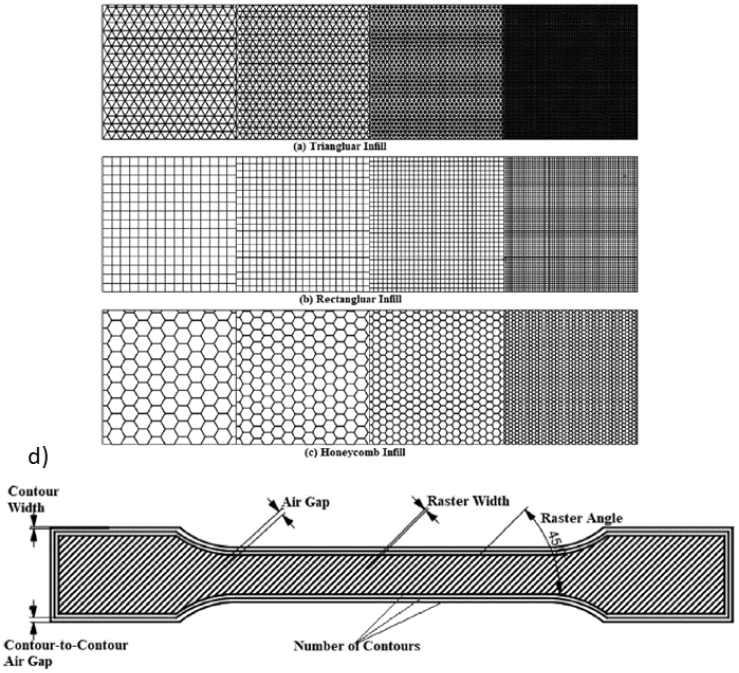

Figure 3.8: a)-c) Different infill patterns and relative density variation. d) Schematic illustration of some typical parameters of the infill patterns made of parallel lines. Reproduced with permission from [71]. Copyright 2019, Elsevier Ltd.

The output of the Ultimaker Cura software is a G-code file, which contains all the instructions for the printer necessary for the realization of each layer of the object. The FDM printer hardware is remotely controlled through the Repetier Host software, in which the G-code file generated by Ultimaker Cura is imported. The Repetier Host software allows also the instructions of the G-code file to be edited and modified. Such possibility was exploited to control the movement of the building plate from the FDM to the ES systems. To this purpose, the following instructions were added to the G-code file content, which allows the movement along the Y-Axis of the building plate:

G1 Y200 F3000

G1 Y

G1 Y200

G1 Y

G1 Y200

G1 Y

3.3.2 Electrospinning System

The ES setup developed in this thesis has a vertical configuration as schematized in figure 2.7. The syringe needle is positively biased by means of an high voltage (HV) power supply (mod. FJ60P02.0-22, Glassman High Voltage Inc., figure 3.6), whereas the building plate (ES collector) can be either grounded or connected to a negative HV power supply (mod. FJ15N08.0-22, Glassman High Voltage Inc.). The HV applied between the needle and the collector can be varied in the interval 0-75 kV.

The 5 mL syringe is filled with the polymer solution and connected to a dual syringe pump (mod. Pump 33, Harvard Apparatus) which allows a constant flow rate through the needle to be established. Typically a 21 gauge needle is used and the flow rate during ES process was varied in the interval 0-1 mL/h. The syringe and the needle are connected by plastic tubes, shielded by using a grounded metallic sheath. A safety valve is placed between the syringe and the needle to prevent the damage of the plastic tubes in case of accidental increase of the pressure. The distance between the needle and the collector was varied in the range 6-18 cm, by using a translation stage on which the needle is mounted.

3.4 Methods for Samples Characterization

3.4.1 Optical Microscope

The morphology of the electrospun fiber and of the samples printed by DIW was investigated by using an optical inverted microscope (mod. IX71, Olympus, figure 3.9). The microscope can operate either in bright field or in fluorescence mode.

The microscope is equipped with a tungsten-halogen lamp for bright field transmitted light microscopy and a mercury vapor arc-discharge lamp for fluorescence microscopy. In bright field mode the samples are illuminated from the top and the

Figure 3.9: Optical Inverted Microscope. Mod. IX71, Olympus.

light transmitted by the sample is collected by the selected microscope objective. The microscope is equipped with 10×, 20×, 40× and 60× objectives, which are located below the specimen. The transmitted light is directed either to the microscope eyepieces or to a CMOS camera for acquiring the samples images.

In fluorescence mode the light coming from the excitation lamp is directed onto the sample through an excitation filter and a dichroic mirror, in order to select specific excitation ranges of wavelengths. There are three available configurations, enabling excitation with UV, blue and green light, respectively. Excitation light is focused onto the sample by the selected objective of the microscope. The fluorescence emitted by the sample is collected by the objective in back-scattering and directed either to the microscope eyepieces or to a CMOS camera for acquiring the samples images.

3.4.2 Integrating Sphere

The use of the integrating sphere is a standard technique for measuring the quantum yield of photoluminescence [72, 73]. In this work it was used to measure the absorption coefficient of samples printed by FDM and made of Vetroalfa, following the method reported in [72, 73]. The integrating sphere is a hollow sphere whose inner surface is coated with a diffusive material (typically barium sulfate) in order to redistribute isotropically light from an external source irrespective of its angular distribution [72, 73]. A broadband lamp (Ocean Optics) is used as the light source. The output light is coupled to an optical fiber (mod. M28L02, Thorlabs). The fiber output light beam is focused onto the sample through a lens. In addition, a diode laser (Micro Laser System, Inc.) with emission wavelength at 408 nm was used as the light source. The sample is placed in an integration sphere (Labsphere). The spectra are measured by using a fiber-coupled monochromator (mod. Flame, Ocean Optics). A photograph of the setup is shown in figure 3.10. Two different measurements were made to obtain the absorption coefficient of the sample, as schematized in figure 3.11. In the first configuration the sample is placed inside the sphere and the light beam is directed onto the sphere wall (figure 3.11a). In the second configuration the light beam is directed onto the sample (figure 3.11b). The absorption coefficient A, can be derived by the following expression [72]:

$$A = (1 - \frac{L_b}{L_a}) \tag{3.2}$$

where $L_{a,b}$ refers to the light intensity measured in the configuration of figure 3.11a,b, respectively.

3.4.3 Characterization of Electrical Properties

In order to measure the electrical resistance of the printed graphene/PLA samples, Current-Voltage (I-V) measurements were carried out. Two centimeters long graphene/PLA samples were printed with cross-sectional area of 0.01 cm^2 and thin Cu wires with a layer of silver epoxy (Chemtronics CW2400, RS) were used at their edges to establish electrical contacts. At least two graphene/PLA samples for each

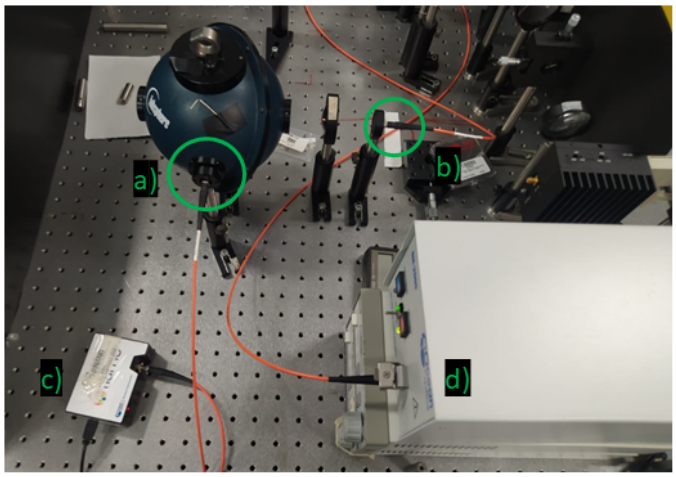

Figure 3.10: Setup used in laboratory for measuring absorption coefficient: a) Output of the sphere connected to the monochromator; b) TORLABS fiber focused into the sphere; c) Monochromator; d) Broad-spectrum lamp

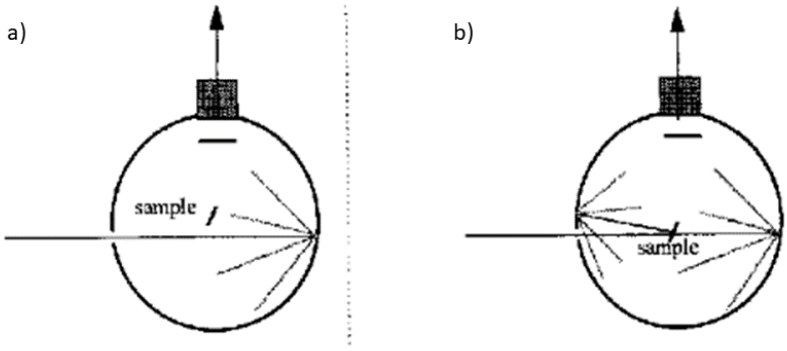

Figure 3.11: Schematic illustration of the two configurations useful for measurement of the absorption absorption coefficient of a sample performed with the integrating sphere: a) the sample is inside the sphere and the beam of the light source is directed onto the sphere wall; b) the beam of the light source is directed onto the sample. Reproduced with permission from [72]. Copyright 1997, Wiley-VCH Verlag GmbH & Co. KGaA.

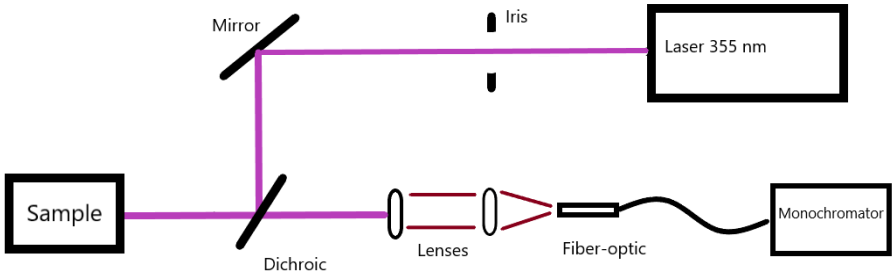

Figure 3.12: Schematization of the ND:Yag laser setup used in this work.

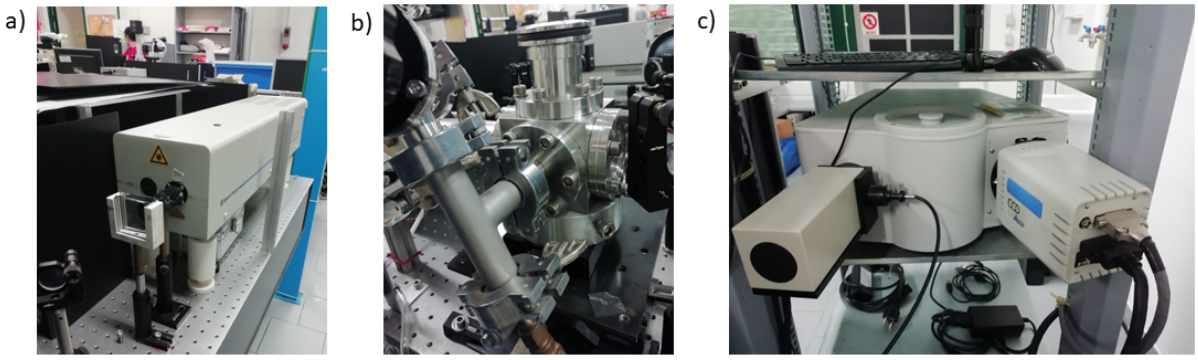

Figure 3.13: a) Nd:Yag laser. c) Vacuum chamber in which the sample is mounted. d) Monochromator with CCD.

selected processing temperature were prepared and each sample was tightly fixed onto a glass substrate by adhesive tape. A Precision Source Meter Unit (B2911A, Keysight Technologies) was used to measure the I-V curves.

3.4.4 Characterization of Lasing Properties

The lasing properties of the samples were characterized by exciting the samples with a Nd:YAG laser (figure 3.13a), which is a solid-state laser that uses a neodymium-doped yttrium-aluminum garnet (YAG) crystal as the active medium. The third harmonic at 355 nm was used for sample excitation. The laser emits a pulsed beam at 10 Hz (pulse duration about 7ns). The setup used is schematized in figure 3.12. The Nd:YAG laser beam passed through an iris with variable aperture (used to define the size of the excitation beam) and was directed onto the sample by a dichroic mirror. The sample is mounted in a stainless steel chamber connected to a mechanical vacuum pump (figure 3.13). The light emitted by the sample is collected in a back-scattering configuration by two lenses and coupled to an optical fiber connected

to monochromator (mod. iHR320, Jobin Yvon, figure 3.13c). The monochromator is equipped with three gratings (600, 900, 1200 grooves/mm) that are mounted in a triple-grating turret. The spectrometer has a Symphony charge coupled device (CCD) detection system (1024x256 pixels), which provides spectra of the emission with high sensitivity, high speed, low noise and reliability for many spectroscopic applications.

4 Experimental Results

This Chapter will focus on the experimental results of the implementation of the 3DP and ES processes and of the characterization of the morphological and optical properties of the realized samples. In the first part of the Chapter, samples made by 3DP with different materials and electrospun NFs will be presented. In particular, the morphological analysis of electrospun NFs by varying the process parameters will be illustrated.

In the second part of the Chapter results concerning the characterization of samples realized through the combination of 3D printing and ES will be presented. RhB was added to the PVA/water solution as the light-emitting chromophore. First, the fabrication process combining 3DP and ES will be presented. Afterwards, a morphological analysis of RhB/PVA electrospun NFs will be illustrated. Finally, optical and lasing emission properties of hybrid samples made of disordered arrays of electrospun NFs deposited on substrates made by 3DP will be discussed.

4.1 3D Printing Implementation

The first part of the experimental work focused on the setup for the 3DP process with the aim of determining the experimental variables that allow for the realization of 3D structures which better reproduce the original design. The printing parameters were optimized starting from those provided by the manufacturer. For all the materials used in this thesis, the following methodology was implemented: a 3D test sample (width: 20mm, length: 20mm, thickness: 1mm, figure 4.1a) was printed by varying the extruder temperature at a fixed bed temperature, and vice versa. The parameters kept fixed for the realization of the test samples were the infill pattern (parallel lines) and the infill density (100%) as schematized in figure 4.1b,c. The realized samples were then analyzed by using an optical microscope for morphological analysis.

4.1.1 3D Printing of Vetroalfa

The first 3D printed material was Vetroalfa, for which the manufacturer suggests an interval for the extruder temperature (T_{ext}) of 210-230 °C and for the bed temperature (T_{bed}) of 70-90 °C. Regarding the bed temperature range, the minimum value of the explored range was 100 °C, because the filament did not adhere to the printing platform for T_{bed} <100 °C. Keeping fixed the extruder temperature at 230 °C, the bed temperature was varied in the 100-110 °C range, with steps of 2 °C. The analysis of the printed samples with the optical microscope evidenced the presence of defect-free structures for T_{bed}=110 °C. Therefore, the bed temperature was set at 110 °C for the realization of the 3D structures of Vetroalfa. Keeping fixed the bed temperature (T_{bed} =110 °C), the extruder temperature was varied in the interval 175-260 °C in steps of 5 °C. First, the measurement of the object macroscopic size (length, width and height) with a caliper evidenced that the geometry of the design was faithfully reproduced within the experimental error (±50μm). The morphology of the printed samples was then analyzed with the optical microscope. In the 175-215 °C range the printed filaments are not continuous as can be seen in figure 4.1d where the bright field optical microscope images of the central area of the printed sample is shown. For the extruder temperature in the range 220-240 °C, the printed filaments retain their filamentary shape once deposited and the sample does not present irregularities (figure 4.1e). By looking at the morphology of the samples printed with the extruder temperature in the range 245-260 °C, some irregular and deformed structures are present in the central area of the samples (figure 4.1f), i.e. the individual filaments were not fully distinguishable and appear flattened. Indeed, by measuring the thickness of the samples in the central area, a decrease of 50±10 μm is found for those samples printed at T_{ext}>245 °C with respect to those printed at T_{ext}= 230 °C. In addition, samples printed at 260 °C displayed a less uniform thickness across the samples, which was evaluated by measuring the sample thickness at the sample edges and in the central area. While for the sample realized at T_{ext}= 230 °C the thickness varied in a range of 20 μm, for the sample realized at T_{ext}= 260 °C such variation is twofold increased. Therefore, was set a value of the extruder temperature of 230 °C for the realization of the 3D structures of Vetroalfa,

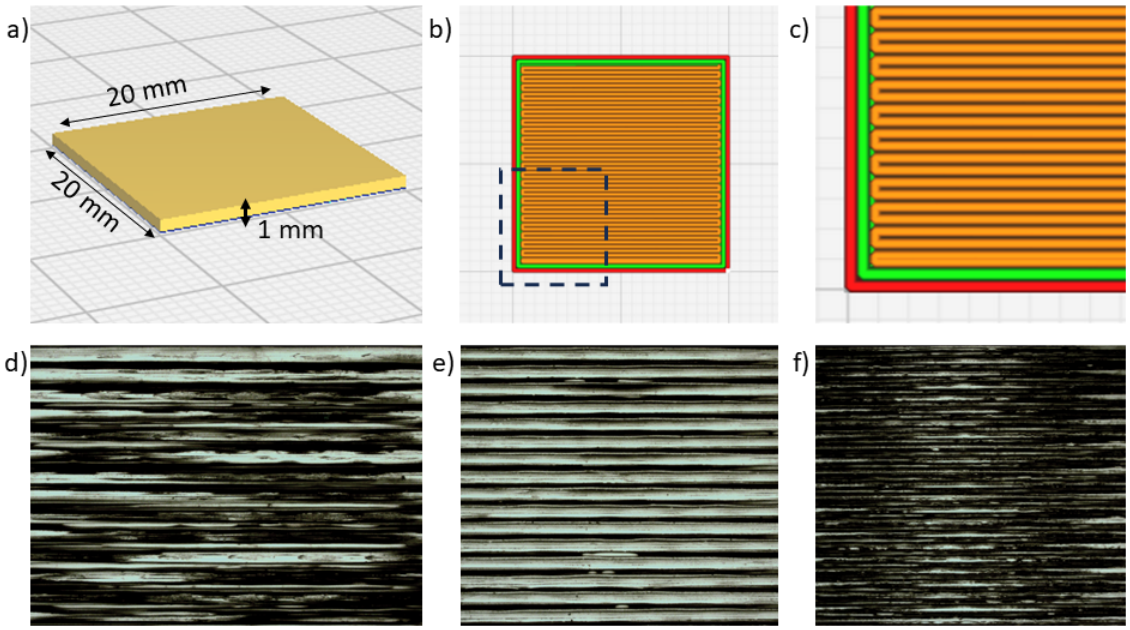

Figure 4.1: a) CAD design of the test sample of size 20mm×20mm×1mm. b) Schematics of a single layer obtained after the slicing process by setting "parallel lines" as infill pattern and 100% as infill density. c) Magnified view of the area inside the dashed rectangle shown in figure b). d-f) Bright field optical microscope images of the central area of the test sample printed by varying the extruder temperature: d) T_{ext}= 190 °C, e) T_{ext}= 220 °C, f) T_{ext}= 260 °C.

i.e. the average value of the temperature range in which the 3D printed samples feature more uniform morphology. By using the samples realized for the optimization of printing parameters, the absorption coefficient of 3D printed structures made of Vetroalfa was measured. For this purpose, the integrating sphere was used with the setup described in figure 3.10 and three set of measurements were performed for each sample in the visible range (400-850 nm). The absorption coefficient was found to be 4.0±0.7% at 408 nm.

Examples of various 3D structures printed with Vetroalfa are shown in figure 4.2. Samples in figure 4.2e,f show the same design 3D printed varying the parameters of the infill density, i.e. an infill distance of 5 mm and 1 mm, respectively. The parameter infill distance is here varied to control the ratio, ρ, of the solids to voids within the volume of the object.

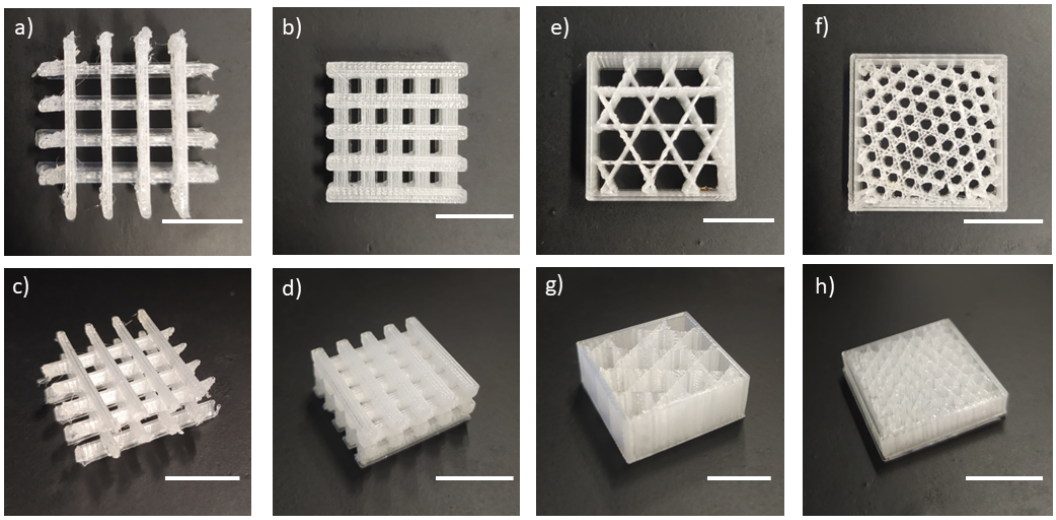

Figure 4.2: a)-h) Photographs of various 3D components made by the Vetroalfa polymer and printed through the FDM technique. Scale bars: 10 mm. Experimental parameters: extrusion temperature 230 °C; bed temperature 110 °C; X,Y translation speed 40 mm/s; thickness of single layer 0.1 mm.

4.1.2 3D Printing of Graphene/PLA composite

Another material used in this work is a graphene/PLA nanocomposite, which allows for 3D printing electrically conductive structures. The manufacturer indicates for T_{ext} and T_{bed} parameters the values of 220 °C and 50 °C, respectively. With the suggested extruder temperature, T_{bed} was varied in the 40-60 °C range, in steps of 5 °C. The choice of this interval of T_{bed} was motivated by the observation that for T_{bed}<40 °C the filament did not adhere to the building plate, whereas for $T_{bed}\geq$60 °C it was difficult to remove the printed object from the building plate without damage. With 45 °C$\leq T_{bed}\leq$55 °C, the filament adhered properly to the building plate and it was not difficult to remove the object when completed. Therefore, the bed temperature was fixed at 50 °C, i.e. the average of the considered interval. This value of T_{bed} experimentally determined is in agreement with that suggested by the manufacturer of the graphene/PLA filament (see table 3.4). By keeping fixed T_{bed}= 50 °C, T_{ext} was varied in the 210-250 °C range, in steps of 5 °C. The choice of the temperature range is due to the fact that for T_{ext}<210 °C and T_{ext}>250 °C, the filament was not extruded continuously. In the 220-240 °C interval, printed filaments retained their shape once deposited, and the realized objects did not presents irregularities.

Therefore, the optimized T_{ext} parameter was 230 °C, the average value of the considered interval. Figure 4.3 shows samples 3D printed with graphene nanocomposite, varying the infill pattern and infill distance, that is 1 mm in figure 4.3a, 2 mm in in figure 4.3b, 4 mm in figure 4.3c and 5 mm in 4.3d. As previously discussed for the samples printed with Vetroalfa, the variation of the infill parameters allows the ratio, ρ, of the solid to void structures to be varied. The electrical resistance of the printed graphene/PLA was measured by printing samples with cross-sectional area of 1mm×1mm and length 20mm. The corresponding I-V curves were measured by using the Precision Source Meter Unit (B2911A, Keysight Technologies) as described in Chapter 3. Figure 4.4 shows an example of the results obtained for samples printed at T_{ext} of 230 °C. Black lines are the linear fits to the data for each measurement. At least two different samples were printed for each set of printing parameters, and for each sample the I-V measurements were repeated two times. In table 4.1 the range of values of the resistance obtained for samples printed at two temperatures of the extruder are reported. The resistance values obtained for the samples printed with an extruder temperature of 230 °C feature a larger spread than the ones of the samples printed at 220 °C. This could be related to the uniformity of internal structure of the printed samples and to a greater variability of size (cross sectional area and length) of the samples printed at 230 °C. For instance the cross-sectional area varies by up to 20% from sample to sample for those printed with T_{ext}=230 °C, with respect to a 5% of variation found for the samples printed with T_{ext} =220 °C. By considering the obtained values of resistance and the measured size of each sample a range of values for the resistivity was obtained: 1.5-2.6 Ωcm. These values are of the same order of magnitude of those found in [66].

Extruder temperature (°C)	Range of values of resistance (Ω)
220	340-360
230	270-450

Table 4.1: Range of values of resistance for graphene/PLA samples printed with different extruder temperatures.

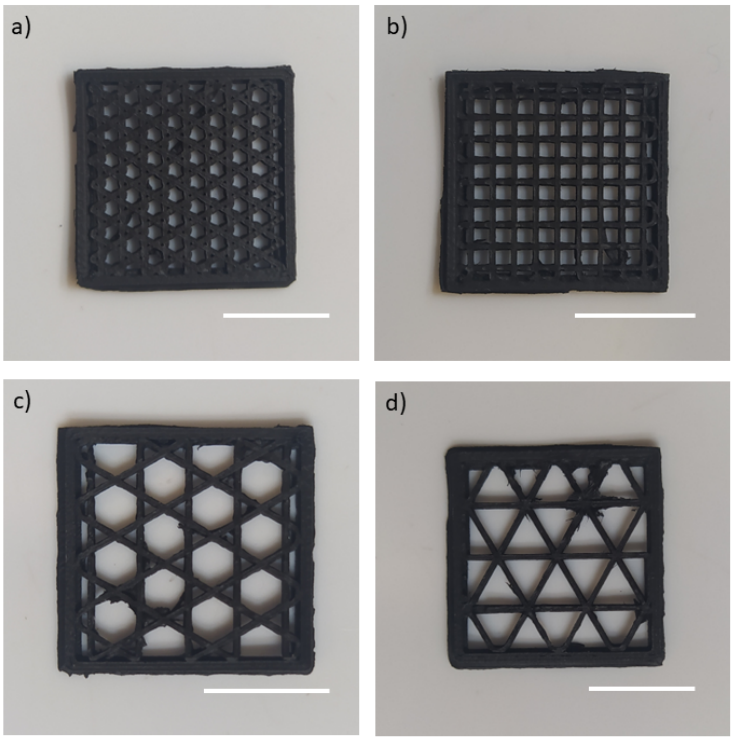

Figure 4.3: a)-d) Photographs of 3D components made of the graphene-polymer nanocomposite. The components are printed by FDM technique. Scale bars: 10 mm. Experimental parameters: extrusion temperature 230 °C; bed temperature 50 °C; X,Y translation speed 40 mm/s; thickness of single layer 0.1 mm.

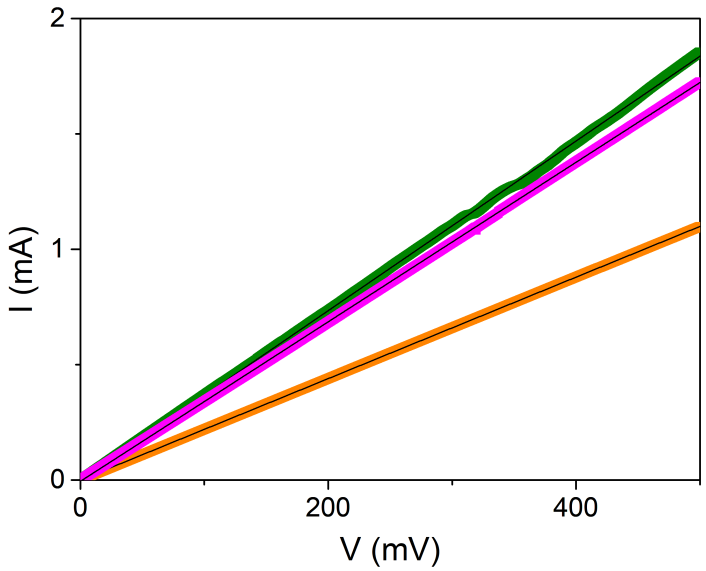

Figure 4.4: I-V curves of three 3D printed graphene/PLA samples with size: cross section 1mm×1mm, length 20mm. The samples were printed with a temperature of the extruder of 230 °C. Other experimental parameters: bed temperature 60 °C; X,Y translation speed 40 mm/s; thickness of single layer 0.1mm. The black lines are linear fits to the data.

4.1.3 3D Printing of nanocomposite PLA

Another material used in this thesis is the PLACTIVE^{TM} filament (figure 4.5), a composite copolymer with antibacterial properties as described in Chapter 3. As printing parameters, the PLACTIVE^{TM} manufacturer indicates the range 190-210 °C for T_{ext} and 0-60 °C for T_{bed}. By fixing T_{ext}= 210 °C, T_{bed} was varied in the range 45-65 °C, in steps of 5°C. The choice of such range of temperature is due to the observation that for T_{ext}<45 °C, there did not adhere to the building plate, while samples printed with $T_{bed}\geq$65 °C are deformed and damaged when removed from the building plate. With 50 °C< T_{bed}<60 °C, the filament adhered properly to the building plate and it was not difficult to remove the object from the plate. The optimized T_{bed} is 55 °C, the central value of this range. Keeping fixed the bed temperature to 55 °C, the extrusion printing temperature was varied in the range 190-210 °C, in steps of 5 °C. The choice of such temperature interval is due to the observation that for T_{ext}<190 °C the filament was not extruded, while for T_{ext}>210

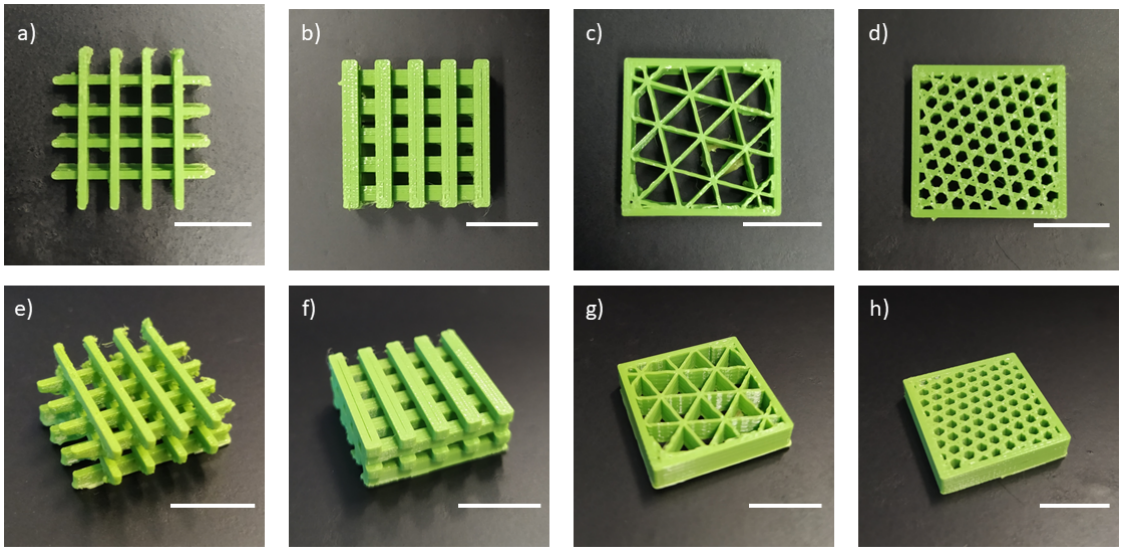

Figure 4.5: a)-h) Photographs of various 3D components made by PLACTIVE^{TM} nanocomposite polymer and printed by the FDM technique. Scale bars: 10 mm. Experimental parameters: extrusion temperature 210 °C; bed temperature 60 °C; X,Y translation speed 40 mm/s; thickness of single layer 0.2 mm.

°C, the printed filament showed irregular shape as visible by naked eyes. In the 190-200 °C interval the filament was not deposited properly on the building plate, because of adhesion to the printing nozzle. In the range 205-210 °C, the 3D design was printed without appreciable defects.

Figure 4.5 shows some examples of structures printed with PLACTIVE^{TM}. In figure 4.5c,d the same structure is 3D printed varying the infill distance, 5mm and 1mm respectively. For investigating the antimicrobial properties of the printed structures a collaborative research is ongoing at the University of Pisa. To this purpose, it will be interesting to investigate the impact of the 3D shape and infill pattern/density on the antimicrobial properties of the 3D printed structures.

4.2 Morphological Analysis of Electrospun Nanofibers

Before characterizing the 3DP and ES combined process, the dependence of the diameter of electrospun NFs on the variation of the main ES parameters was analyzed. The main ES process parameters that can be varied are: the solution concentration, the bias voltage, the needle-to-collector distance and the flow rate. The morphological analysis was carried out by using a scanning electron microscope. The diameter

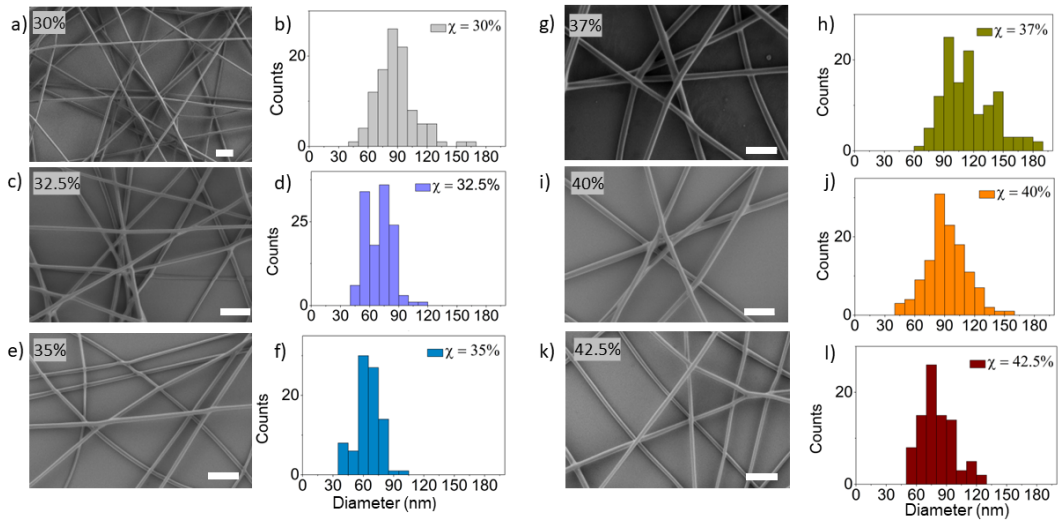

Figure 4.6: a),c),e),g),i),k) SEM micrographs of nanofibers electrospun at different PVA/water concentrations, χ, and b),d),f),h),j),l) corresponding diameter distributions. Scale bar of SEM micrographs: 500 nm. Other experimental parameters: PVA Mw: 13.000-23.000 g/mol; applied voltage 19 kV; flow rate 0.2 mL/h; needle-to-collector distance 12 cm.

distribution was obtained by measuring the diameter of $\simeq$ 100 fibers for each set of electrospinning parameters. This procedure was made by using SEM images and the software "ImageJ" for their analysis.

In the first part of this Section, the results on NFs made of PVA with a molecular weight of 13.000-23.000 g/mol dissolved in distilled water will be presented.

First, the variation of PVA/water concentration, χ, was analyzed, keeping all others parameters fixed. The concentration (χ), considered as the weight ratio between PVA and water, was varied in the interval 30% - 42.5%. For concentrations lower than 30% continuous fibers were not formed and electrospray was observed. For concentrations>42.5% the PVA polymer was not completely dissolved in water. The results of this analysis are shown in figure 4.6. Figures 4.6a,c,e,g,i,j show SEM micrographs of nanofibers electrospun with the PVA/water concentration indicated in the corresponding inset. Figures 4.6b,d,f,h,j,l show the nanofibers diameter distributions for each concentration. Table 4.2 summarizes the results of the analysis.

Another parameter varied is the flow rate. Six different values were investigated in the interval 0.1-1 mL/h, keeping fixed the other parameters. Figures 4.7a,c,e,g,i,k show the SEM micrographs of nanofibers for different flow rates, as indicated in the

Concentration of PVA in H_2O (mg/mL)	Flow rate (mL/h)	Spinneret-to-collector distance (cm)	Voltage (kV)	Average diameter (nm)
30 %	0.2	12	19	80 ± 10
32.5 %	0.2	12	19	90 ± 20
35 %	0.2	12	19	110 ± 30
37 %	0.2	12	19	60 ± 10
40 %	0.2	12	19	60 ± 10
42.5 %	0.2	12	19	90 ± 20
37 %	0.1	12	19	80 ± 20
37 %	0.2	12	19	110 ± 30
37 %	0.4	12	19	90 ± 20
37 %	0.6	12	19	80 ± 20
37 %	0.8	12	19	80 ± 20
37 %	1	12	19	70 ± 10

Table 4.2: Process parameters and resulting fiber diameters (expressed as the average $\pm$ the standard deviation calculated from the distribution of fiber diameters) for the six different PVA (Mw: 13.000-23.000 g/mol) concentrations and flow rate used for the electrospinning process. The parameter that is varied is shown in orange background, all the others are fixed.

corresponding insets. Figures 4.7b,d,f,h,j,l show the the NFs diameters distribution for the different values of the flow rate. The others parameters used for this analysis are summarized in table 4.2.

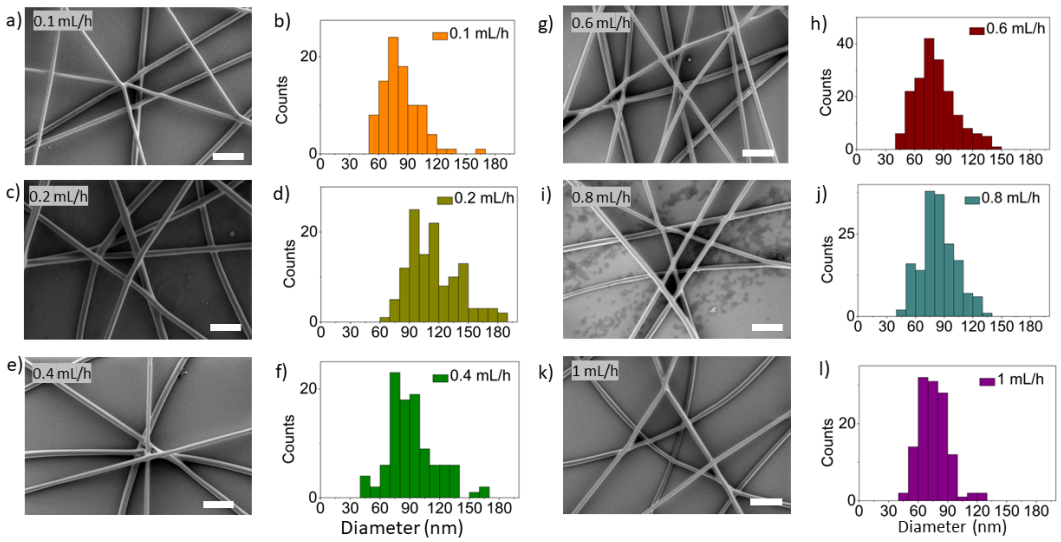

Figure 4.7: a),c),e),g),i),k) SEM micrographs of nanofibers electrospun at different flow rates and b),d),f),h),j),l) corresponding diameter distributions. Scale bar of SEM micrographs: 500 nm. Other experimental parameters: PVA Mw 13.000-23.000 g/mol; applied voltage 19 kV; $\chi = 37\%$ PVA/water w/w; needle-to-collector distance 12 cm.

Figures 4.8a,c,e,g show SEM micrographs for NFs electrospun varying the needle-to-collector distance in the range 9-18 cm, and figures 4.8b,d,f,h the relative diameters distribution. The ES parameters used for this analysis are summarized in table 4.3.

Finally, another parameter that influences the average diameter of electrospun NFs is the voltage applied between the needle and the collector. The voltage is varied in the interval 9-17 kV and other parameters are kept fixed. Figures 4.9a,c,e,g,i,k show SEM micrograph of NFs electrospun varying the applied voltage and figures 4.9b,d,f,h,j,l show the corresponding diameter distributions. The ES parameters used for this analysis are reported in table 4.3.

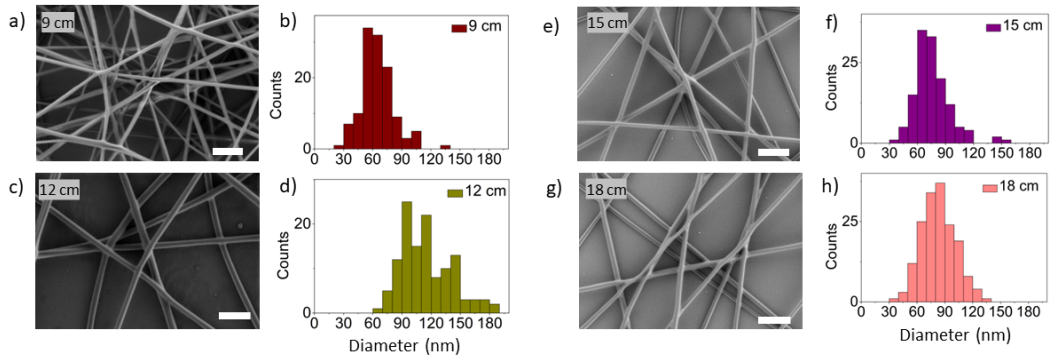

Figure 4.8: a),c),e),g) SEM micrographs of NFs electrospun at different needle-to-collector distance and b),d),f),h) corresponding diameter distributions. Scale bar of SEM micrographs: 500 nm. Other experimental parameters: PVA Mw 13.000-23.000 g/mol; applied voltage 19 kV; $\chi = 37\%$ PVA/water w/w; flow rate 0.2 mL/h.

Concentration of PVA in H_2O (mg/mL)	Flow rate (mL/h)	Spinneret-to-collector distance (cm)	Voltage (kV)	Average diameter (nm)
37 %	0.2	6	19	70 ± 20
37 %	0.2	9	19	60 ± 20
37 %	0.2	12	19	110 ± 20
37 %	0.2	15	19	70 ± 20
37 %	0.2	18	19	80 ± 20
37 %	0.2	12	9	50 ± 30
37 %	0.2	12	11	70 ± 20
37 %	0.2	12	13	70 ± 20
37 %	0.2	12	15	80 ± 20
37 %	0.2	12	17	70 ± 20

Table 4.3: Process parameters and resulting fiber diameters (expressed as the average ± the standard deviation calculated from the distribution of fiber diameters) for the five different needle-to-collector distance and applied voltage used for the electrospinning process. The parameter that is varied is shown in orange background, all the others are fixed.

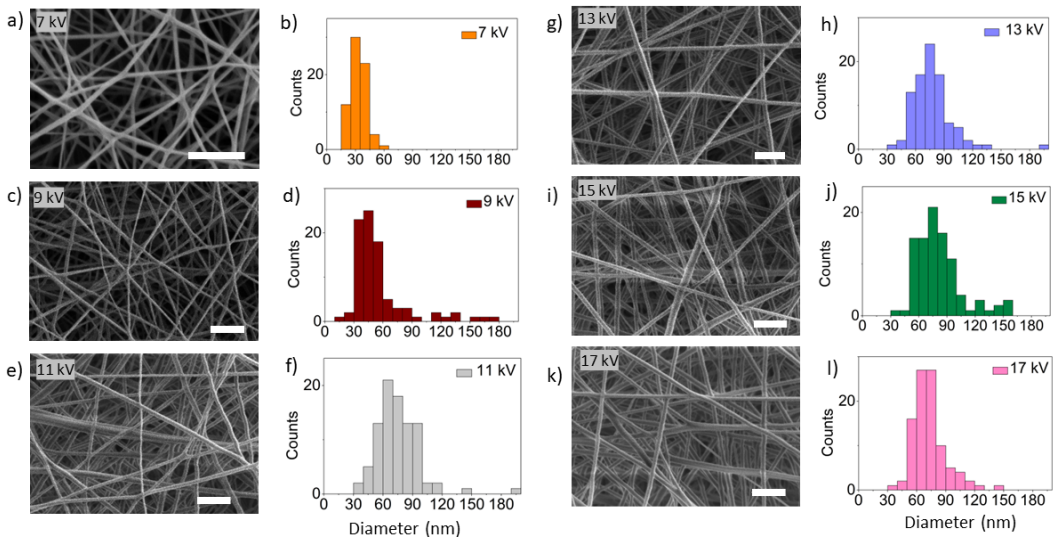

Figure 4.9: a),c),e),g),i),k) SEM micrographs of NFs electrospun varying the applied voltage and b),d),f),h),j),l) corresponding diameter distributions. Scale bar of SEM micrographs: 500 nm. Other experimental parameters: PVA Mw 13.000-23.000 g/mol; needle-to-collector distance 12 cm; χ = 37% PVA/water w/w; flow rate 0.2 mL/h.

Overall, the previous experimental investigation shows that the average diameter of the NFs electrospun with PVA, Mw 13.000-23.000 g/mol, is of about 80 nm, a value that appears to be quite stable in the range of process variables investigated. Coupling of light emitted by the fluorescent molecules embedded in the NFs to the waveguide modes and the waveguiding of light through the NFs are highly important for light amplification and the achievement of laser emission [8]. Therefore, the size of the electrospun NFs must be suitable for the propagation of single or few optical modes. An estimation of the NF diameter matching the previous requirements can be derived by considering the condition for the transition from single to multimode operation of optical fibers, that is [74]: $V_N = (\frac{\pi d}{\lambda})(n_{nf}^2 - n_0^2)^{0.5}$=2.405, where d is the NF diameter, n_{nf} is the NF refractive index and n_0 is the air refractive index. λ is the wavelength of light propagating through the NF, that is around 630 nm for the system investigated in this thesis (i.e. the wavelength at which the light-emitting molecules feature optical gain as will be shown in the following). The fluorescent nanofibers are made by PVA, which has a refractive index of 1.463 [75]. The previous condition allows for estimating a diameter, d_w, around which few modes can propagates through the NF, that is $d_w \simeq$450 nm. Moreover, for NF diameter close

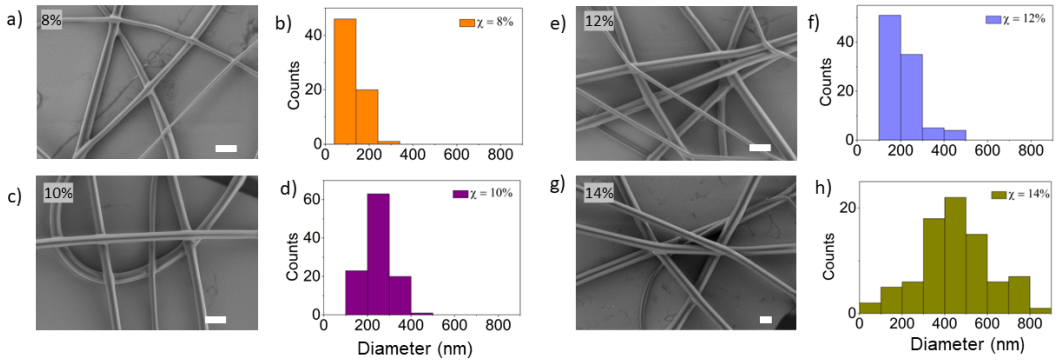

Figure 4.10: a),c),e),g) SEM micrographs of NFs electrospun at different PVA/water concentrations, χ, and b),d),f),h) corresponding diameter distributions. Scale bar of SEM micrographs: 500 nm. Other experimental parameters: PVA Mw 85.000-124.000 g/mol; applied voltage 23 kV; flow rate 0.2 mL/h; needle-to-collector distance 12 cm.

to d_w the coupling of light emitted by the fluorescent species to the modes of the NF is also more efficient, as recently demonstrated for electrospun NFs embedding single emitters [76]. The results presented above regarding the variation of the ES process parameters, evidenced that the NFs diameter is lower than the size required for few mode waveguiding in all the investigated range of parameters.

In [77] the PVA Mw was varied in the interval 9.000-124.000 g/mol and the resulting NFs average diameter was in the interval 250 nm - 2 μm. Based on the results of this work, PVA with Mw of 85.000-124.000 g/mol was used for the ES process, by dissolving this polymer in distilled water at different concentrations in the range 8-14% w/w.

Figures 4.10a,c,e,g show the SEM micrographs of NFs electrospun at different PVA/water concentrations and figures 4.10b,d,f,h show the relative diameters distribution. The ES parameter with which nanofibers were electrospun are summarized in table 4.4.

In figure 4.11 the average diameter of NFs as a function of the solution concentration is shown. The data show a 180% increase in diameter by varying the PVA/water w/w concentration in the range 8-14%. Moreover the average diameters of the NFs obtained by increasing the PVA Mw are higher than those realized by the one obtained initially by using the PVA with lower Mw and, more importantly, at the higher solution concentration fibers with diameters (460 $\pm$ 170 nm) suitable for light coupling and optical waveguiding for luminescence at 630 nm were realized.

Cocentration of PVA 85.000-124.000 Mw in H_2O (mg/mL)	Flow rate (mL/h)	Spinneret-to-collector distance (cm)	Voltage (kV)	Average diameter (nm)
8 %	0.2	12	23	120 ± 40
10 %	0.2	12	23	240 ± 60
12 %	0.2	12	23	210 ± 60
14 %	0.2	12	23	450 ± 170

Table 4.4: Process parameters and resulting NF diameters (expressed as the average $\pm$ the standard deviation calculated from the distribution of fiber diameters) for the four different PVA (Mw: 85.000-124.000 g/mol) concentrations used for the electrospinning process. The parameter that is varied is shown in orange background, all the others are fixed.

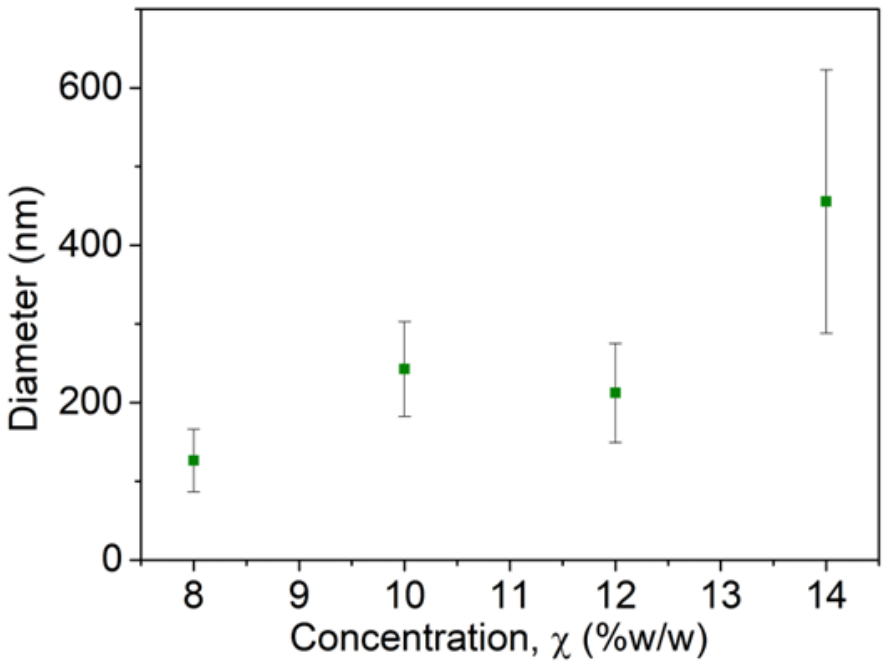

Figure 4.11: NFs average diameter as a function of the PVA/water concentration, χ. Other experimental parameters: PVA Mw 85.000-124.000 g/mol; applied voltage 23 kV; flow rate 0.2 mL/h; needle-to-collector distance 12 cm.

The trend of the values of the average diameters that is shown in figure 4.11 is due to the fact that by increasing the polymer concentration, the entanglements of the macromolecular component and the viscosity of the solution increase, making the stretching of the polymer jet relatively less effective [77].

4.3 Combination of 3DP and ES Processes

As a first structure composed by electrospun NFs and 3D printed components, an hybrid sample consisting of a NFs mat suspended between two 3D printed frames was realized. The 3D printed frames have a structure of 20mm×20mm×3mm with a 4mm hole in the center, in which the NFs remain suspended. Initially, Vetroalfa was used for 3D printing and a solution made of 37% PVA (Mw: 13.000-23.000 g/mol)/water w/w concentration was electrospun. The 3D printed frame consisted on 29 layers (0.1 mm thick). For NFs deposition, the 3D printing process was suspended after the first 15 layers (figure 4.12a), when the whole printed structure has reached a height of 1.5 mm. This height allows the NFs not to adhere to the copper collector once deposited. Once the first 15 layers of Vetroalfa were printed, the building plate was moved to the ES station (figure 4.12b). After the deposition of NFs on top of the 3D printed frame, the building plate was moved back to the 3D printing station (figure 4.12c) and the solvent is allowed to evaporate, by keeping the temperature of the building plate at the one used for printing (110 °C). Finally, the last 14 layers were printed on top of the deposited NFs mat (figure 4.12d). The hybrid sample realized following the procedure described above is shown in figure 4.12e-h. The geometry of the 3D frame here presented was chosen with the idea of exploiting this architecture in view of realizing hybrid samples capable of laser emission by electrospinning fluorescent nanofibers onto the 3D frame. In fact, it would allows a better confinement of light emitted by the dye in the electrospun fibers, due to the higher refractive index contrast between the PVA polymer matrix and the surrounding air (n_{nf} - n_0 = 0.463, where n_0 is the refractive index of air) with respect to NFs deposited on the glass substrate (n_{nf} - n_{glass} = 0.057, where n_{glass} is the refractive index of BK7 glass [78]). In addition, the 3D frame allows for better manipulation of the NFs mat thanks to the 3D printed support.

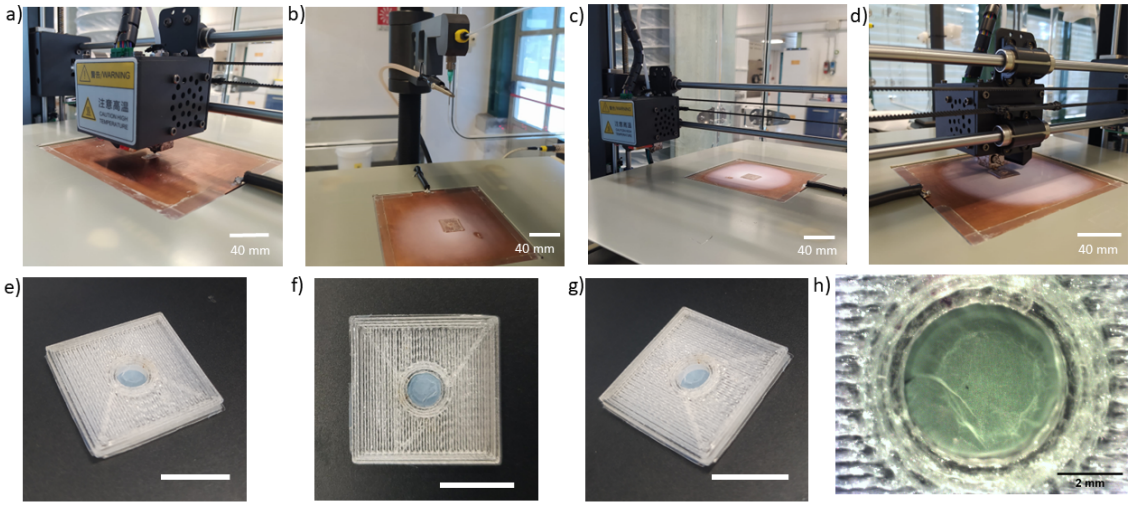

Figure 4.12: Fabrication of hybrid samples. a) 3D printing of the first 15 layers of Vetroalfa polymer by FDM. b) Electrospinning of a nanofiber array on top of the 3D printed structure. c) The printing platform is moved back to the 3D printing area. d) 3D printing of the 14 layers of Vetroalfa on top of the nanofibers. Scale bars of a)-d) 40 mm. e)-g) Photographs of the hybrid sample. Scale bars: 10 mm. h) Optical microscope image of the hybrid sample. 3D Printing parameters: extrusion temperature 230 °C; bed temperature 110 °C; X,Y translation speed 40 mm/s; thickness of single layer 0.1 mm. Electrospinning parameters: Mw of the PVA 13.000-23.000 g/mol; Concentration, χ, of PVA in water w/w 37%; applied voltage 19 kV; flow rate 0.2 mL/h; needle-to-collector distance 12 cm.

4.4 Morphological Analysis of Hybrid Samples

The architecture of the hybrid sample shown in figure 4.12e-h was exploited to realize hybrid samples capable of lasing emission. To this aim, RhB was added to the PVA (Mw: 85.000-124.000 g/mol)/water solution as a fluorescent molecule. A solution made of 14% PVA/water w/w and 1% RhB/PVA w/w was realized. After the addition of RhB, an optimization of the electrospinning parameters was carried out in order to obtain continuous electrsopun NFs. Keeping the other parameters fixed, the voltage was varied until nanofibers without beads were obtained. The optimized ES parameters for the RhB/PVA/water solution were: flow rate 0.2 mL/h, applied voltage 12 kV, needle-to-collector distance 12 cm.

Three hybrid samples with the architecture similar to the sample in figure 4.12e-h were realized by 3D printing the frame with graphene/PLA composite and electrospinning on top of it the RhB/PVA/water solution. The samples were made varying the nanofibers deposition time from 1 minute up to 10 minutes and the corresponding SEM micrographs are shown in figure 4.13a,b,c. An analysis of the diameters distribution of the NFs electrospun with the parameters listed above was made following the procedure described in Section 4.2, in order to check that the condition $d > d_w$ was still met. To this aim, SEM micrographs of the samples with high magnification (figure 4.13d-h) was used to measure $\simeq 100$ NFs diameters through ImageJ. Figure 4.13h shows the NFs diameter distribution, the average value of which is 500 ± 200 nm. This value is in agreement with that obtained for the nanofibers electrospun with the 14% PVA/water w/w solution.

The NFs deposition time influences the NFs density and thus the average length of the edges of NFs network. Figures 4.14a,b,c show bright-field optical microscope images of the samples shown in figure 4.13a,b,c, respectively. The corresponding fluorescence confocal microscope images were used to evaluate the mean length of the edge of NFs network (figure 4.14d,e,f). This was done by averaging over 100 edges measured between two different network nodes, as schematized in figure 4.14e. As shown in figure 4.15, the average edge length of the NFs network decreased by 17% while increasing the deposition time by 10%, from $\simeq 45$ μm down to $\simeq 8$ μm. These results show that the network geometry can be controlled by the ES process

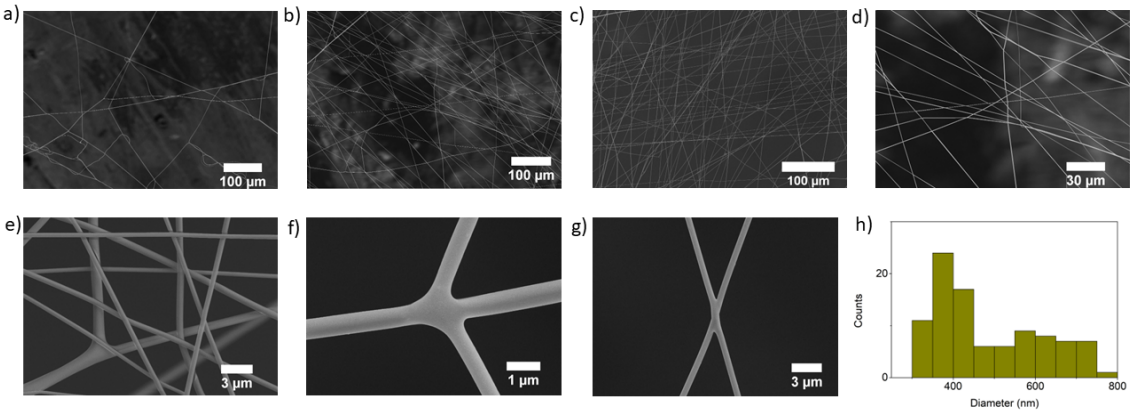

Figure 4.13: a)-c) SEM micrographs of NFs on 3D printed frames obtained by depositing the fibers for a) 1 minute, b) 5 minutes and c) 10 minutes. d)-g) SEM micrographs of NFs with higher magnification. h) Distribution of NF diameters. Other experimental parameters: Mw of the PVA: 85.000-124.000 g/mol; concentration, of PVA/water w/w: 14%, ratio of RhB/PVA w/w: 1%; applied voltage 12 kV; flow rate: 0.2 mL/h; needle-to-collector distance: 12 cm.

variables, a relevant achievement in view of the possibility of varying the lasing properties of the NFs networks through the topology of the network, as shown in Ref.s [8, 79]. These studies showed that the lasing threshold of NFs networks decreases as the network degree increases (see also figure 2.2) and the number of lasing modes can be controlled through the length of the network edges.

In order to verify that the RhB molecule was homogeneously distributed in the electrospun NFs, the fluorescence intensity profile was measured along the length of 10 fibers. This was done by using the dedicated function of ImageJ and exploiting the fluorescence confocal microscope micrographs shown in figure 4.14d,e,f. A variation of 10% over an average NF length of $\simeq 100$ μm was found.

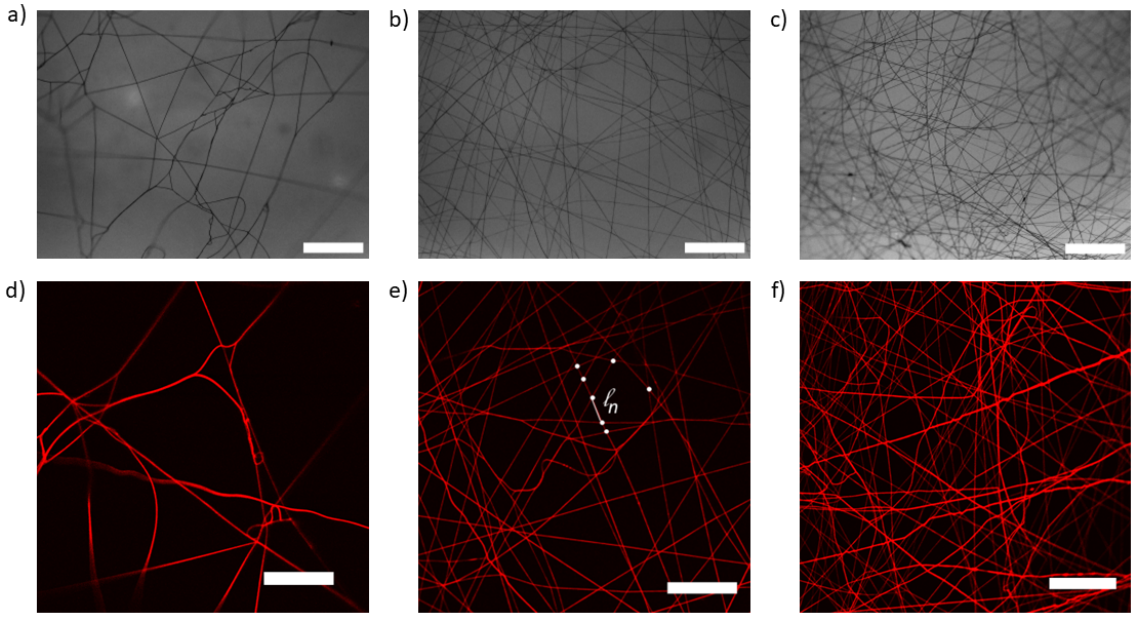

Figure 4.14: a)-c) Bright-field optical microscope images and d)-f) fluorescence confocal microscope images of the NFs mat suspended through a 3D printed frame. Scale bars: a)-c) 200 μm, d)-e) 100 μm. White dots in e) highlight some nodes, while l_n indicates an edge of the nanofiber network. Electrospinning parameters: Mw of the PVA: 85.000-124.000 g/mol; concentration of PVA/water w/w: 14%, ratio of RhB/PVA w/w: 1%; applied voltage 12 kV; flow rate: 0.2 mL/h; needle-to-collector distance: 12 cm. Nanofiber deposition time: 1 min a), 5 min b), 10 min c).

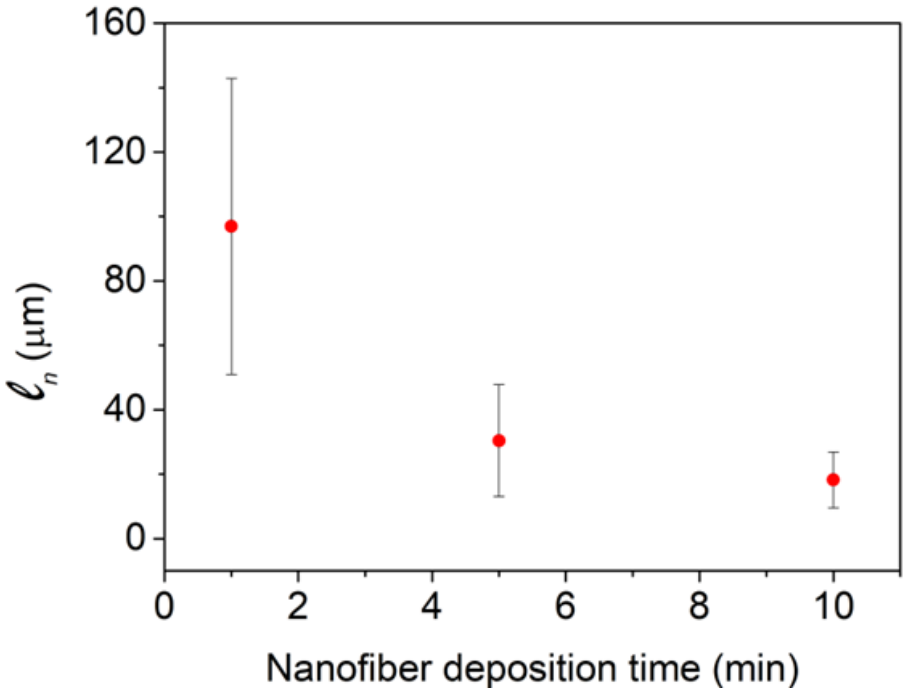

Figure 4.15: Average edge length of the nanofiber network as a function of the nanofiber deposition time. Data are obtained from the images shown in figure 13.

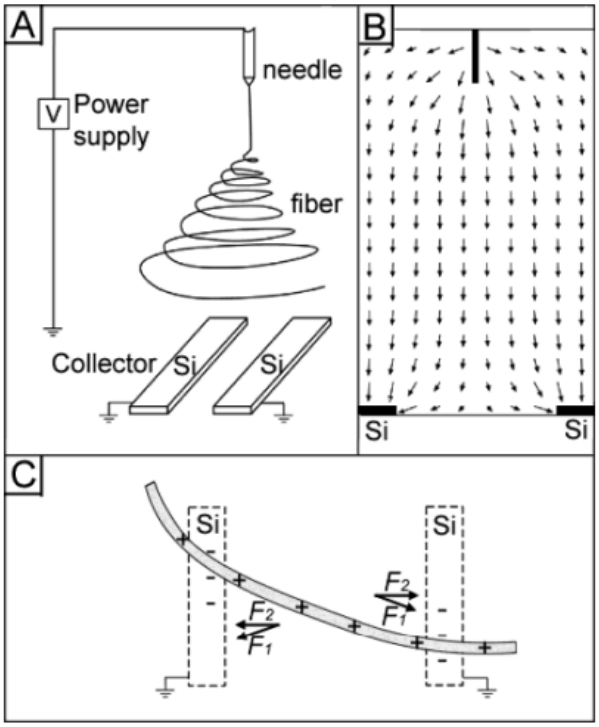

Figure 4.16: a) Schematics of the setup implemented for obtaining uniaxially aligned NFs. In the original set-up implementation, the collector consists on two grounded Si stripes separated by an insulating gap. b) Calculated electric field strength vectors between the needle and the collector. c) Analysis of the forces to which a NFs is subjected near the collector. Reproduced with permission from [80]. Copyright, 2003, American Chemical Society.

Samples with different NFs alignment geometries were then realized. To this aim, the collector was made of graphene/PLA nanocomposite and the collector design was varied in order to obtain NFs arrays with different degree of alignment, following the methodology introduced in Ref. [80]. This was done by 3D printing several structures on an insulating substrate and connecting the printed structures to the negative HV generator. For the NFs to be aligned, the collector should have insulating gaps as schematized in figure 4.16a for two parallel conductive stripes separated by an insulating gap. In such configuration, the electric field lines are modified by the presence of the two electrodes figure 4.16b. The so-generated electric field is at the base of the first type of electrostatic force, (F_1, figure 4.16c), that NFs experience in the ES process when landing on the patterned collector. Figure 4.16b shows that in the proximity of the two electrodes, F_1 pulls the two ends of the fiber toward the two electrodes. The other type of electrostatic force (F_2) to

which NFs are subjected during the ES process is that between the charged fiber and the image charges induced on the surfaces of the grounded electrodes. The net result of F_1 and F_2 causes NFs to be aligned perpendicularly to the edges of the electrodes. In addition, NFs suspended between the two electrodes can remain partially charged. The electrostatic repulsion between the deposited and incoming nanofibers can further promote their parallel alignment [80]. The sample in figure 4.17a consists of a collector made of two graphene/PLA stripes and NFs are mainly aligned perpendicularly to the stripe edges. In figure 4.17b the collector is made of four graphene/PLA stripes positioned at 90° and NFs form a grid in the central gap of the sample shown in the inset (figure 4.17b). The collector used for realizing the sample shown in figure 4.17c is made of an external graphene/PLA ring with a central cylinder [81], and the NFs are mainly aligned radially. Figure 4.17d,e show the fluorescent confocal microscope images of figure 4.17a,b,c, respectively, while figure 4.17f show the fluorescence micrograph of the sample in figure 4.17c.

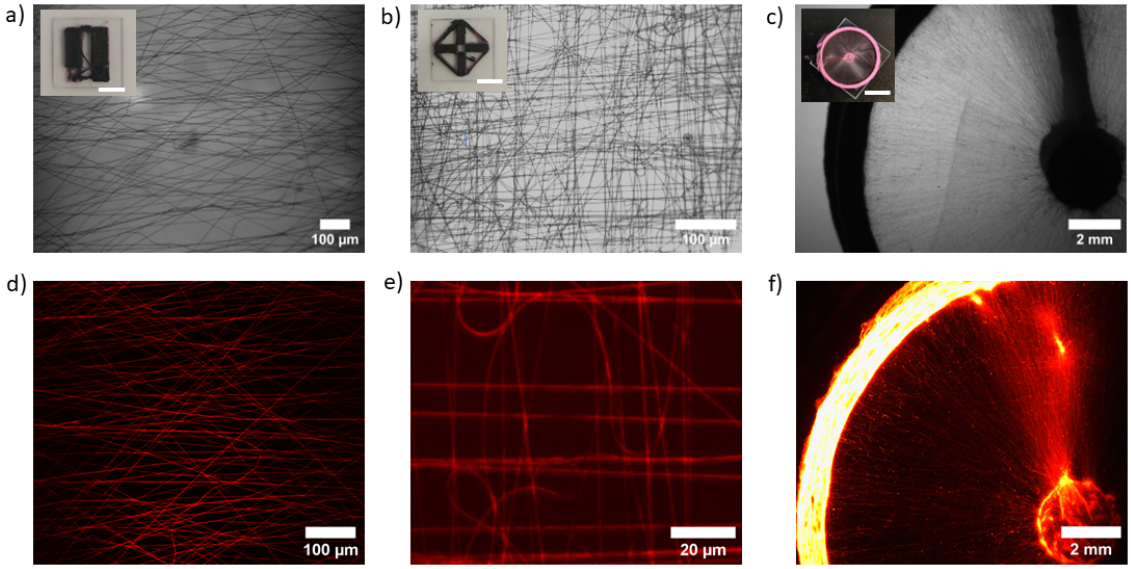

Figure 4.17: Bright-field optical microscope images of NFs deposited on 3D printed frames made of the graphene/PLA with different geometries. The insets show photographs of the samples, respectively. Scale bars of inset: 10 mm. d)-e) Fluorescence confocal microscope images of samples shown in figure a), b), respectively. f) Fluorescence micrograph of the sample shown in figure c). 3DP parameters: Extrusion temperature 235 °C; bed temperature 60 °C; X,Y translation speed 40 mm/s; thickness of single layer 0.2 mm. Electrospinning parameters: Mw of the PVA: 85.000-124.000 g/mol; concentration of PVA/water w/w: 14%, ratio of Rhb/PVA w/w: 1%; applied voltage 12 kV; flow rate: 0.2 mL/h; needle-to-collector distance: 12 cm.

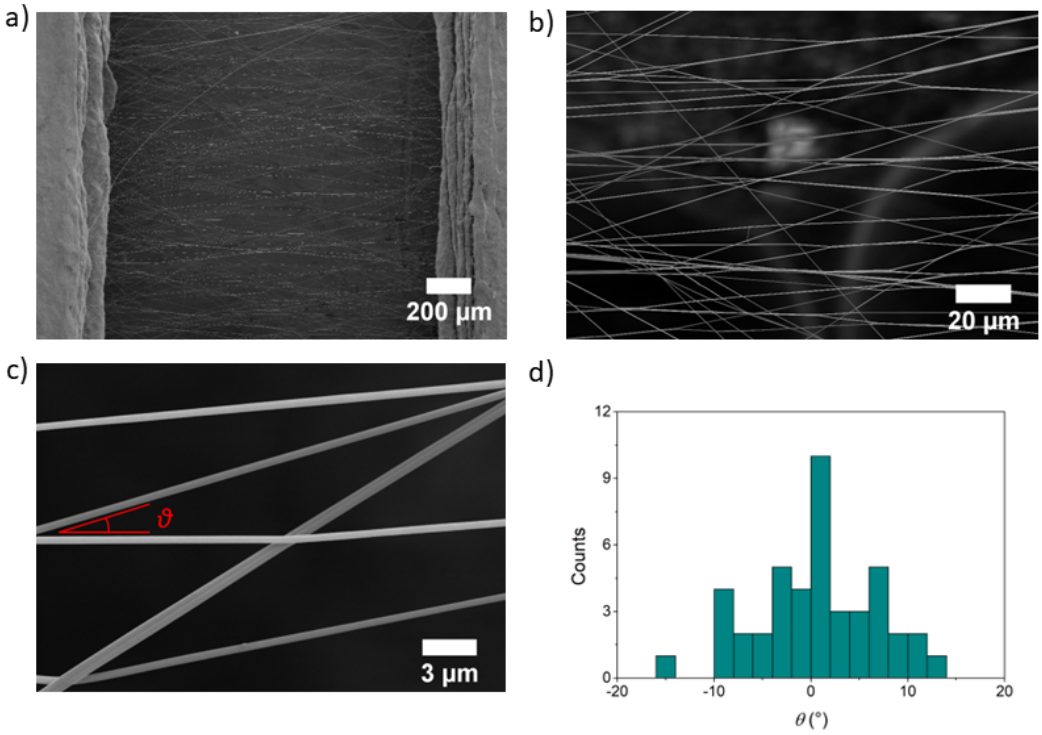

Figure 4.18: a)-c) SEM micrographs of uniaxially aligned nanofibers and d) corresponding distribution of θ. The angle θ is shown in c). Other experimental parameters: Mw of the PVA: 85.000-124.000 g/mol; concentration, of PVA/water w/w: 14%, ratio of RhB/PVA w/w: 1%; applied voltage 12 kV; flow rate: 0.2 mL/h; needle-to-collector distance: 12 cm.

An analysis of the degree of alignment was performed on the uniaxially aligned NFs (sample in figure 4.17a), whose SEM micrographs at different magnifications are shown in figure 4.18a,b,c. The analysis was performed by calculating their angular distribution. Angles were measured by fixing as 0° the direction of a fiber arranged perpendicularly between the two graphene/PLA stripes (inset of figure 4.17a), as schematically represented in figure 4.18c. The results are shown in figure 4.18d. The measured angles are mainly distributed in the range ±10° (i.e. 90% of the NFs form angles in the range ±10° with respect to the direction perpendicular to the graphene/PLA stripes). These results are in line with the angular distributions of uniaxially aligned nanofibers found in other similar works [82], [83] and [84].

4.5 Optical Properties of Hybrid Samples

In this Section the emission properties of networks of randomly oriented RhB/PVA nanofibers will be presented.

A preliminary analysis of the optical properties of the RhB molecule in a PVA matrix was carried out. To this purpose, a RhB/PVA film was deposited on a quartz substrate by spincoating (2000 rpm). Figure 4.19a shows the optical transmission spectrum of the sample, measured by using a spectrophotometer (mod. Lambda 950, Perkin Elmer). The spectrum has a minimum at a wavelength $\simeq$ 557 nm with an overall bandwidth of about 60 nm. These features can be attributed to RhB absorption [85]. The RhB/PVA film (that is shown in the inset of figure 4.19a) was then excited by the Nd:YAG laser at wavelength of 355 nm, with a spot diameter of 3 mm. The setup for this measurement is shown in figure 3.12, while figure 4.19b shows the photoluminescence (PL) spectra measured at two different excitation fluences. At lower excitation fluence (1.1 mJ cm^{-2}) the typical spontaneous emission spectrum of RhB was measured (blue curve), which exhibits a first peak around the value of 587 nm, with a bandwidth of 50 nm, and a second less evident peak at wavelength of about 635 nm, in agreement with previous work [86]. By increasing the excitation fluence (2.3 mJ cm^{-2}) an additional narrow peak at $\simeq$ 629 nm (bandwidth of 20 nm) was observed (red curve), that is attributed to amplified spontaneous emission (ASE). ASE is a highly directional and intense emission which occurs when the spontaneous emission of a gain medium is optically amplified by stimulated emission [87], and it is indicative of the wavelength range where the molecule has optical gain. Therefore, laser emission of nanofiber networks is expected to occur in this wavelength range.

The PL spectrum of a NFs sample similar to the one shown in figure 4.14c was measured (figure 4.20). To this aim, the sample (shown in the inset of figure 4.20) was excited with an incident fluence of 1.1 mJ cm^{-2}, using the same setup as that used for the RhB/PVA film. The spectrum has a peak centered around 585 nm with a bandwidth of 60 nm, comparable with the one obtained for the film. The minor differences between the PL spectra of figure 4.19b and figure 4.20 are likely due to the different microenvironment of the RhB molecule in the film and NFs [88].

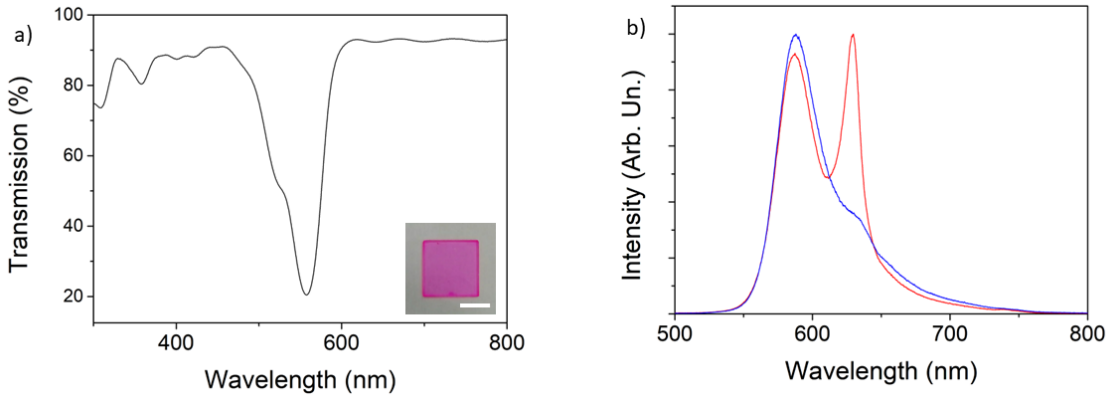

Figure 4.19: a) Optical transmission spectrum of a RhB/PVA/quartz multilayer. A photograph of the sample is shown in the inset. Scale bar: 10 mm. The RhB/PVA film was deposited on a quartz substrate (20mm×20mm×1mm) by spincoating. The thickness of the RhB/PVA film is $2.4 \pm 0.1\mu$m. b) PL spectrum of the sample shown in a) upon optical pumping with the Nd:YAG laser with fluence of 1.1 mJ cm^{-2} (blue line) and 2.3 mJ cm^{-2} (red line).

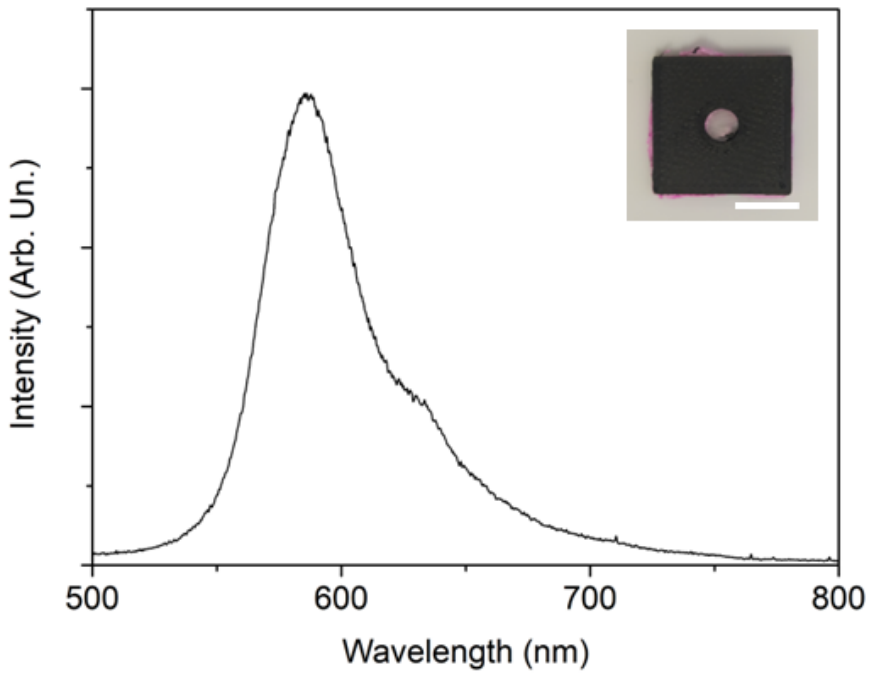

Figure 4.20: PL spectrum of a PVA/RhB NFs mat deposited on a 3D printed frame made of graphene/PLA. The sample is shown in the inset (scale bar: 10 mm). Excitation fluence of 1.1 mJ cm^{-2}. Electrospinning parameters: Mw of the PVA: 85.000-124.000 g/mol; concentration of PVA/water w/w: 14%, concentration of Rhb/PVA w/w: 1%; applied voltage 12 kV; flow rate: 0.2 mL/h; needle-to-collector distance: 12 cm.

The emission spectrum of a sample similar to the one shown figure 4.14a was analyzed by optical pumping it with an increasing fluence in the range 0.2-35 mJ cm^{-2}. Figure 4.21a shows the emission spectra of the excited sample. A sharp peak is observed at a wavelength of 639 nm, starting from an incident fluence of 2.7 mJ cm^{-2}. By increasing the incident fluence, the 639 nm peak intensity increases and other peaks start to appear. In figure 4.21b the intensity of the peaks at 639 nm and 640 nm is shown as a function of the excitation fluence (Light-out vs Light-in). A threshold trend characteristic of a laser process can be observed. These results are in agreement with ref. [79], where different lasing modes of the NF network feature different excitation thresholds. In the inset of figure 4.21b the number of emission peaks in the spectral interval 615-650 nm as a function of the excitation fluence is shown. The number of peaks is almost constant for excitation fluences>26.3 mJ cm^{-2}. These results are in line with other theoretical and experimental studies on different random laser systems [89, 90, 91, 92]. Figure 4.22a shows the emission spectra at increasing excitation fluences of a second sample. Figure 4.22b shows the intensity of the peak at a wavelength of 644 nm as a function of the excitation fluence. A threshold trend can be seen and the fluence value estimated as the lasing threshold is 13.4 mJ cm^{-2}. The inset of figure 4.22b shows the number of emission peaks in the spectral interval 620-650 nm as a function of the incident fluence, featuring a trend similar to the one shown in 4.21b.

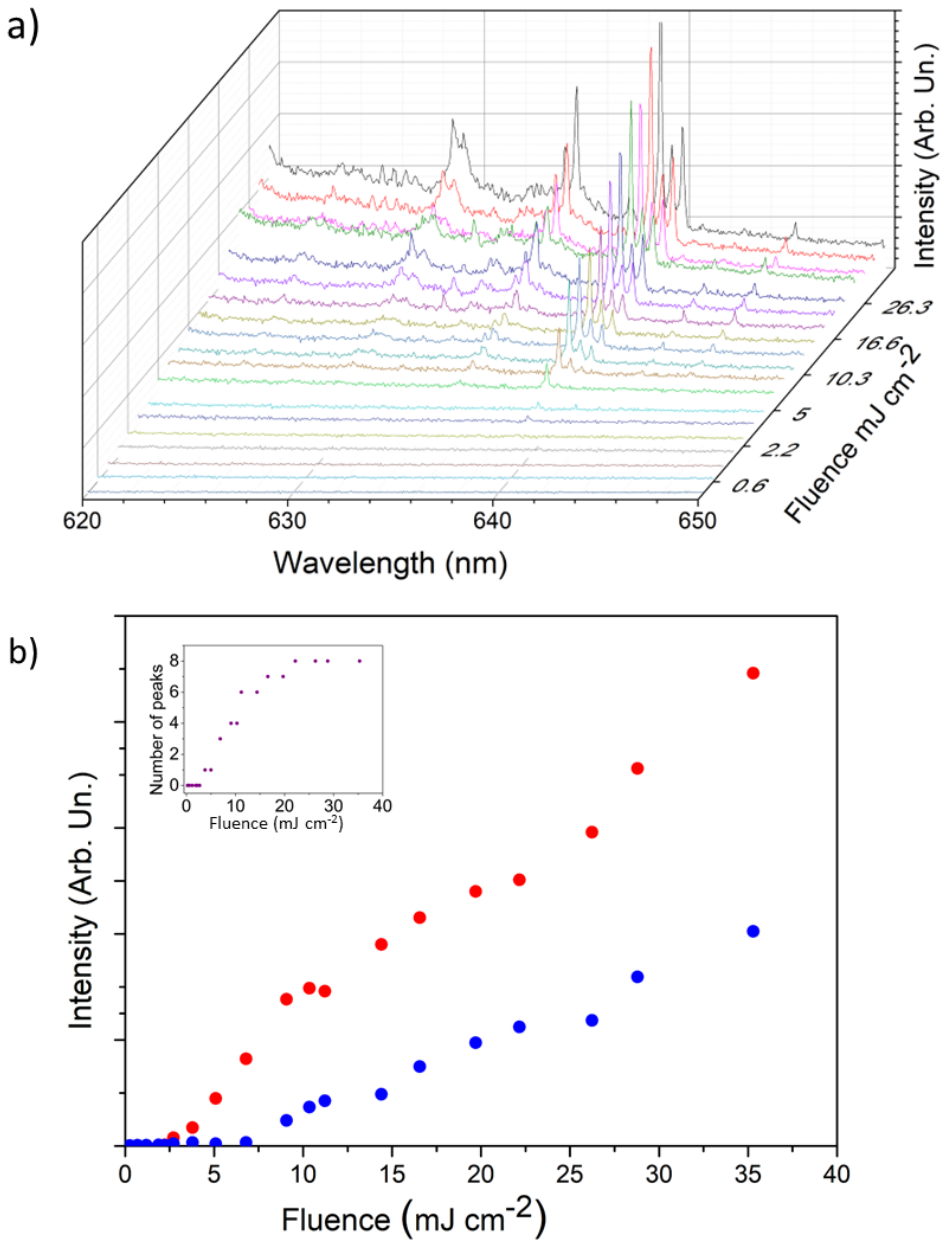

Figure 4.21: a) Emission spectra of a RhB/PVA NFs mat suspended between two 3D printed frame of graphene/PLA as a function of the excitation fluence. b) Emission intensity of the peak at 639 nm (red circles) and 640 nm (blue circles) as a function of the excitation fluence. The inset shows the number of lasing peaks as a function of the excitation fluence.

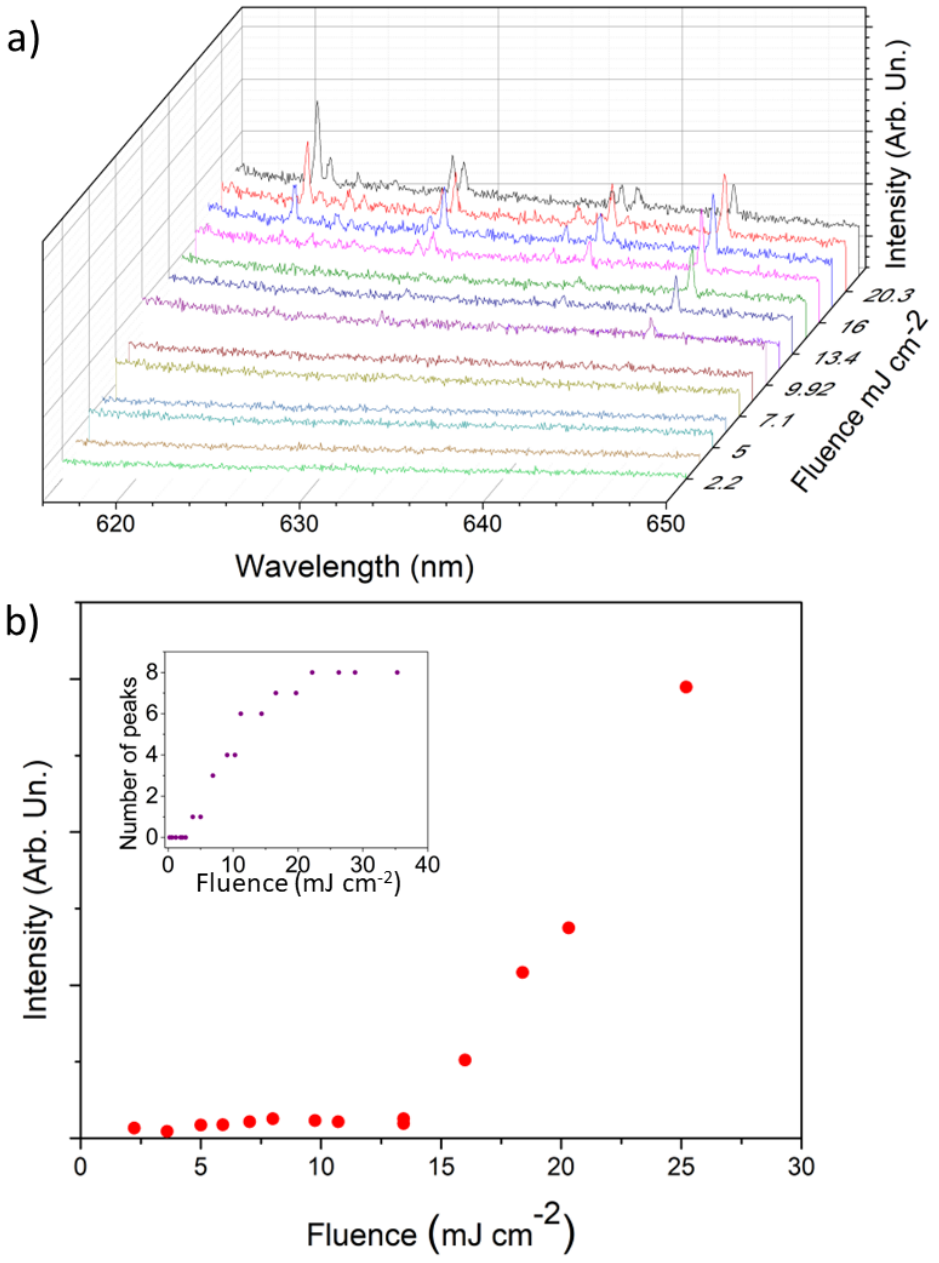

Figure 4.22: a) Emission spectra of a RhB/PVA NFs mat suspended between two 3D printed frame of graphene/PLA as a function of the excitation fluence. b) Emission intensity of the peak at 644 nm wavelength. The inset shows the number of lasing peaks as a function of the excitation fluence.

In [79], high sensitivity of the spectral features of the lasing spectrum of NFs networks to the spatial intensity profile of the pumping beam was observed, by shaping the pumping laser beam through a digital micromirror device (DMD). In this thesis, the shape of the excitation spot was varied by placing different shadow masks in front of the sample while exciting it. The emission spectra were acquired at a fixed excitation fluence (4.5 mJ cm^{-2}) for which laser peaks were present. Figure 4.23 shows three different emission spectra acquired by placing in front of the sample the mask schematized in the corresponding inset. Figure 4.23a shows the emission spectrum acquired by using a transparent mask. It presents two principal peaks: one with higher intensity at a wavelength of 631 nm (red circle), and a second with lower intensity at a wavelength of 633 nm (green circle). The spectrum in figure 4.23b was acquired by placing in front of the sample the mask schematized in the inset and two peaks were still visible. The first one is at a wavelength of 631 nm (red circle) and the second one is at a wavelength of 633 nm (green circle). The circles of the same color indicate the same lasing peak. By changing the shape of the excitation spot, peaks are still visible but their intensity decreased by 40%, while their relative intensity ratio varies from 0.6 to 0.3. Figure 4.23c shows the emission spectra acquired by placing in front of the sample the mask schematized in the inset. In this case the emission peaks disappeared. Before acquiring this spectrum, the transparent mask was placed again to verify that the sample was still emitting. Through this analysis, it was possible to conclude that the laser emission strongly depends on the shape of the exciting spot, a result which opens interesting perspectives for controlling the emission spectrum of NF networks.

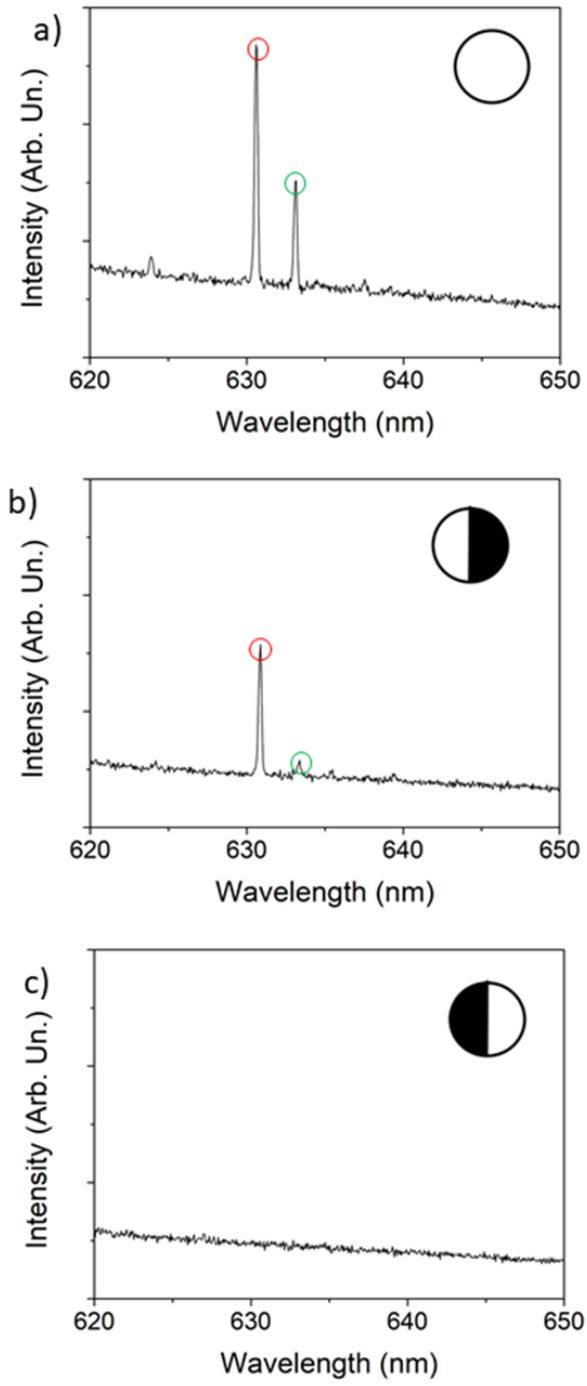

Figure 4.23: a)-c) Emission spectra of a RhB/PVA array of randomly oriented NFs deposited on a 3D printed frame upon varying the shape of the excitation spot by using shadow masks. The shape of the masks is shown in the insets, respectively. In a)-b) the red and green circles indicate the same lasing peak, respectively. Excitation fluence: 4.5 mJ cm^{-2}.

5 Conclusion and Perspectives

The scope of this thesis was the realization of networks of light-emitting NFs with random lasing properties. To this aim, an apparatus capable of manufacturing samples through 3DP and ES was developed. The system was built by modifying an Anycubic i3 Mega FDM printer and adding to it a new ES system. The whole apparatus was placed in a dedicated movable table and enclosed in a plexiglass box. In the first phase of the work, the FDM and ES systems were separately analyzed. In order to characterize the FDM printing process, three different materials (Vetroalfa, graphene/PLA composite and PLACTIVE^{TM}) were used. 3D objects were realized varying the design geometry and the printing parameters. The properties of the printed objects were also studied. For instance, a 3D printed graphene/PLA composite featured a resistivity in the range 1.5-2.6 Ωcm.

The ES technique was used in order to investigate the dependence of the NFs morphology on the process parameters. To this purpose, solutions made of PVA with molecular weight of 13.000-23.000 g/mol dissolved in distilled water were electrospun varying the ES process parameters. An analysis of NFs diameter distribution as a function of the ES parameters was performed, finding average diameters of $\simeq$ 80 nm for all the investigated sets of process parameters. In view of fabricating NFs samples capable of lasing emission, NFs with larger diameter are more favorable for light transport and amplification. To address this, PVA with Mw 85.000-124.000 g/mol dissolved in water was used, allowing for obtaining NFs with an average diameter of 450 $\pm$ 170 nm.

Once the 3DP and ES processes were optimized, a hybrid samples made by two 3D printing frames and a NFs mat between them was realized. In order to realize hybrid samples with fluorescent nanofibers, RhB was added in the PVA (Mw: 85.000-124.000 g/mol)/water solution, as the light emitting component. The average diameter of nanofibers electrospun with such composition was found to be $\simeq$ 500 nm.

Samples made of NFs deposited between 3D printed frames were made by varying the NFs deposition time, a parameter that influences the density of the NFs and the

average length of the edges of NFs network. By increasing the deposition time by 10%, the average edges length decreases by 80%, from $\simeq 45\mu$m to $\simeq 8\mu$m, evidencing the capability of controlling the topology of the NFs network through the ES process parameters.

Arrays of NFs with different mutual alignment configurations (such as uniaxial and radial alignment) were realized by using 3D printed patterned collectors made of graphene/PLA composite. The emission spectra of two hybrid samples of RhB/PVA nanofibers were then measured by increasing the incident excitation fluence in the range $\simeq$ 0.2-35 mJ cm^{-2}. Random lasing peaks were found starting from a threshold fluence of 2.7 mJ cm^{-2}. A dependence of the samples emission spectrum on the shape of the excitation spot was also found.

The hybrid samples realized in this thesis have a great potentiality in the field of nanophotonics, imaging and spectroscopy. The sensitivity of random lasing emission spectrum to the external perturbations can be exploited for optical sensing applications. Thanks to the fabrication system developed in this thesis combining 3DP and ES, random laser sources can be integrated in a 3D printed frame. In perspective the 3D printed frame can be designed in order to collect and waveguide the light emitted by the NFs networks. Moreover, the possibility to vary the network topology found in the present study can be exploited for investigating the influence of the network topology on the lasing properties (e.g. lasing threshold, wavelengths and number of lasing modes).

Furthermore, the combined 3DP and ES system developed in this thesis can also be exploited for biophysical applications. For instance, the possibility of alternating 3DP and ES of biomaterials in a layer-by-layer fashion, could be exploited for the realization of 3D structures with a controlled internal multi-scale architecture, suitable for cells proliferation and growth.

References

[1] K Thyagarajan and Ajoy Ghatak. *Lasers: fundamentals and applications*. Springer Science & Business Media, 2010.

[2] Orazio Svelto, David C Hanna, et al. *Principles Of Lasers*, volume 1. Springer, 2010.

[3] Diederik S Wiersma. The physics and applications of random lasers. *Nature Physics*, 4(5), 2008.

[4] Brandon Redding, Michael A Choma, and Hui Cao. Spatial coherence of random laser emission. *Optics Letters*, 36(17), 2011.

[5] Alice Boschetti, Andrea Taschin, Paolo Bartolini, Anjani Kumar Tiwari, Lorenzo Pattelli, Renato Torre, and Diederik S Wiersma. Spectral super-resolution spectroscopy using a random laser. *Nature Photonics*, 14(3), 2020.

[6] Brandon Redding, Michael A Choma, and Hui Cao. Speckle-free laser imaging using random laser illumination. *Nature Photonics*, 6(6), 2012.

[7] Francesca Matino, Luana Persano, Andrea Camposeo, and Dario Pisignano. Laser systems and networks with organic nanowires and nanofibers. *Advanced Optical Materials*, 7(17), 2019.

[8] Michele Gaio, Dhruv Saxena, Jacopo Bertolotti, Dario Pisignano, Andrea Camposeo, and Riccardo Sapienza. A nanophotonic laser on a graph. *Nature Communications*, 10(1), 2019.

[9] Dario Pisignano. *Polymer nanofibers: building blocks for nanotechnology*. Number 29. Royal Society of Chemistry, 2013.

[10] Tomasz Kozior, Al Mamun, Marah Trabelsi, and Lilia Sabantina. Comparative analysis of polymer composites produced by fff and pjm 3d printing and electrospinning technologies for possible filter applications. *Coatings*, 12(1), 2022.

[11] Izabella Rajzer, Anna Kurowska, Adam Jabłoński, Samuel Jatteau, Mateusz Śliwka, Magdalena Ziąbka, and Elżbieta Menaszek. Layered gelatin/plla scaffolds fabricated by electrospinning and 3d printing-for nasal cartilages and subchondral bone reconstruction. *Materials & Design*, 155, 2018.

[12] Victor Chausse, Enric Casanova-Batlle, Cristina Canal, Maria-Pau Ginebra, Joaquim Ciurana, and Marta Pegueroles. Solvent-cast direct-writing and electrospinning as a dual fabrication strategy for drug-eluting polymeric bioresorbable stents. *Additive Manufacturing*, 2023.

[13] Christian Mendoza-Buenrostro, Hernan Lara, and Ciro Rodriguez. Hybrid fabrication of a 3d printed geometry embedded with pcl nanofibers for tissue engineering applications. *Procedia Engineering*, 110, 2015.

[14] Yuan-Yuan Liu, Hong-Chen Yu, Yi Liu, Gang Liang, Ting Zhang, and Qing-Xi Hu. Dual drug spatiotemporal release from functional gradient scaffolds prepared using 3 d bioprinting and electrospinning. *Polymer Engineering & Science*, 56(2), 2016.

[15] Faraz Fazal, Francisco Javier Diaz Sanchez, Muhammad Waqas, Vasileios Koutsos, Anthony Callanan, and Norbert Radacsi. A modified 3d printer as a hybrid bioprinting-electrospinning system for use in vascular tissue engineering applications. *Medical Engineering & Physics*, 94, 2021.

[16] Jianghui Dong, Ru-Jhang Jhu, Liping Wang, Cho-Pei Jiang, and Cory J Xian. A hybrid platform for three-dimensional printing of bone scaffold by combining thermal-extrusion and electrospinning methods. *Microsystem Technologies*, 2019.

[17] Tao Xu, Kyle W Binder, Mohammad Z Albanna, Dennis Dice, Weixin Zhao, James J Yoo, and Anthony Atala. Hybrid printing of mechanically and biologically improved constructs for cartilage tissue engineering applications. *Biofabrication*, 5(1), 2012.

[18] Riccardo Sapienza. Determining random lasing action. *Nature Reviews Physics*, 1(11), 2019.

[19] Soocheol Kim, SungYeun Yang, Seung Ho Choi, Young L Kim, WonHyoung Ryu, and Chulmin Joo. Random lasing from structurally-modulated silk fibroin nanofibers. *Scientific Reports*, 7(1), 2017.

[20] R Zhang, S Knitter, SF Liew, FG Omenetto, BM Reinhard, H Cao, and L Dal Negro. Plasmon-enhanced random lasing in bio-compatible networks of cellulose nanofibers. *Applied Physics Letters*, 108(1), 2016.

[21] Sven Gnutzmann and Uzy Smilansky. Quantum graphs: Applications to quantum chaos and universal spectral statistics. *Advances in Physics*, 55(5-6), 2006.

[22] Van Duong Ta, Rui Chen, Lin Ma, Yong Jun Ying, and Han Dong Sun. Whispering gallery mode microlasers and refractive index sensing based on single polymer fiber. *Laser & Photonics Reviews*, 7(1), 2013.

[23] Naisa Chandrasekhar and Rajadurai Chandrasekar. Reversibly shape-shifting organic optical waveguides: formation of organic nanorings, nanotubes, and nanosheets. *Angewandte Chemie*, 124(15), 2012.

[24] Carmela De Marco, Elisa Mele, Andrea Camposeo, Ripalta Stabile, Roberto Cingolani, and Dario Pisignano. Organic light-emitting nanofibers by solvent-resistant nanofluidics. *Advanced Materials*, 20(21), 2008.

[25] Yun-Tzu Hsu, Yen-Yu Lin, Yi-Zih Chen, Hsia-Yu Lin, Yu-Ming Liao, Cheng-Fu Hou, Min-Hsuan Wu, Wei-Ning Deng, and Yang-Fang Chen. 3d printed random lasers. *Advanced Materials Technologies*, 5(1), 2020.

[26] Andrea Camposeo, Luana Persano, Maria Farsari, and Dario Pisignano. Additive manufacturing: applications and directions in photonics and optoelectronics. *Advanced Optical Materials*, 7(1), 2019.

[27] Corson L Cramer, Emanuel Ionescu, Magdalena Graczyk-Zajac, Andrew T Nelson, Yutai Katoh, Jeffery J Haslam, Lothar Wondraczek, Trevor G Aguirre,

Saniya LeBlanc, Hsin Wang, et al. Additive manufacturing of ceramic materials for energy applications: Road map and opportunities. *Journal of the European Ceramic Society*, 2022.

[28] Tuan D Ngo, Alireza Kashani, Gabriele Imbalzano, Kate TQ Nguyen, and David Hui. Additive manufacturing (3d printing): A review of materials, methods, applications and challenges. *Composites Part B: Engineering*, 143, 2018.

[29] Jill Z Manapat, Qiyi Chen, Piaoran Ye, and Rigoberto C Advincula. 3d printing of polymer nanocomposites via stereolithography. *Macromolecular Materials and Engineering*, 302(9), 2017.

[30] Samuel Clark Ligon, Robert Liska, Jurgen Stampfl, Matthias Gurr, and Rolf Mulhaupt. Polymers for 3d printing and customized additive manufacturing. *Chemical Reviews*, 117(15), 2017.

[31] Frederik Kotz, Karl Arnold, Werner Bauer, Dieter Schild, Nico Keller, Kai Sachsenheimer, Tobias M Nargang, Christiane Richter, Dorothea Helmer, and Bastian E Rapp. Three-dimensional printing of transparent fused silica glass. *Nature*, 544(7650), 2017.

[32] Jennifer A Lewis. Direct ink writing of 3d functional materials. *Advanced Functional Materials*, 16(17), 2006.

[33] Du T Nguyen, Cameron Meyers, Timothy D Yee, Nikola A Dudukovic, Joel F Destino, Cheng Zhu, Eric B Duoss, Theodore F Baumann, Tayyab Suratwala, James E Smay, et al. 3d-printed transparent glass. *Advanced Materials*, 29(26), 2017.

[34] Hyunwoo Yuk and Xuanhe Zhao. A new 3d printing strategy by harnessing deformation, instability, and fracture of viscoelastic inks. *Advanced Materials*, 30(6), 2018.

[35] Tao Jiang, Jose G Munguia-Lopez, Salvador Flores-Torres, Jacqueline Kort-Mascort, and Joseph M Kinsella. Extrusion bioprinting of soft materials: An

emerging technique for biological model fabrication. *Applied Physics Reviews*, 6(1), 2019.

[36] Ibrahim T Ozbolat and Monika Hospodiuk. Current advances and future perspectives in extrusion-based bioprinting. *Biomaterials*, 76, 2016.

[37] Jill K Sherwood, Susan L Riley, Robert Palazzolo, Scott C Brown, Donald C Monkhouse, Matt Coates, Linda G Griffith, Lee K Landeen, and Anthony Ratcliffe. A three-dimensional osteochondral composite scaffold for articular cartilage repair. *Biomaterials*, 23(24), 2002.

[38] Damian M Kirchmajer, R Gorkin Iii, et al. An overview of the suitability of hydrogel-forming polymers for extrusion-based 3d-printing. *Journal of Materials Chemistry B*, 3(20), 2015.

[39] Tali Re'em, Orna Tsur-Gang, and Smadar Cohen. The effect of immobilized rgd peptide in macroporous alginate scaffolds on tgfβ1-induced chondrogenesis of human mesenchymal stem cells. *Biomaterials*, 31(26), 2010.

[40] P Selcan Gungor-Ozkerim, Ilyas Inci, Yu Shrike Zhang, Ali Khademhosseini, and Mehmet Remzi Dokmeci. Bioinks for 3d bioprinting: an overview. *Biomaterials Science*, 6(5), 2018.

[41] Tao Jiang, Jose G Munguia-Lopez, Salvador Flores-Torres, Jacqueline Kort-Mascort, and Joseph M Kinsella. Extrusion bioprinting of soft materials: An emerging technique for biological model fabrication. *Applied Physics Reviews*, 6(1), 2019.

[42] Samuel Clark Ligon, Robert Liska, Jurgen Stampfl, Matthias Gurr, and Rolf Mulhaupt. Polymers for 3d printing and customized additive manufacturing. *Chemical Reviews*, 117(15), 2017.

[43] Betina Madeira Schmitt, Christiano Fraga Zirbes, Cassiano Bonin, Daniel Lohmann, Diovani Castoldi Lencina, and Aurélio da Costa Sabino Netto. A comparative study of cartesian and delta 3d printers on producing pla parts. *Materials Research*, 20, 2018.

[44] Nandana Bhardwaj and Subhas C Kundu. Electrospinning: A fascinating fiber fabrication technique. *Biotechnology Advances*, 28(3), 2010.

[45] Wee E Teo and Seeram Ramakrishna. A review on electrospinning design and nanofibre assemblies. *Nanotechnology*, 17(14), 2006.

[46] Hao Fong and Darrell H Reneker. Investigation of the formation of carbon and graphite nanofiber from mesophase pitch nanofiber precursor. ACS Publications, 2006.

[47] Tomasz Kozior, Al Mamun, Marah Trabelsi, and Lilia Sabantina. Comparative analysis of polymer composites produced by fff and pjm 3d printing and electrospinning technologies for possible filter applications. *Coatings*, 12(1), 2022.

[48] Izabella Rajzer, Anna Kurowska, Adam Jabłoński, Samuel Jatteau, Mateusz Śliwka, Magdalena Ziąbka, and Elżbieta Menaszek. Layered gelatin/plla scaffolds fabricated by electrospinning and 3d printing-for nasal cartilages and subchondral bone reconstruction. *Materials & Design*, 155, 2018.

[49] Dan-Lei Yang, Fazal Faraz, Jie-Xin Wang, and Norbert Radacsi. Combination of 3d printing and electrospinning techniques for biofabrication. *Advanced Materials Technologies*, 7(7), 2022.

[50] Christian Mendoza-Buenrostro, Hernan Lara, and Ciro Rodriguez. Hybrid fabrication of a 3d printed geometry embedded with pcl nanofibers for tissue engineering applications. *Procedia Engineering*, 110, 2015.

[51] Yuan-Yuan Liu, Hong-Chen Yu, Yi Liu, Gang Liang, Ting Zhang, and Qing-Xi Hu. Dual drug spatiotemporal release from functional gradient scaffolds prepared using 3 d bioprinting and electrospinning. *Polymer Engineering & Science*, 56(2), 2016.

[52] Jianghui Dong, Ru-Jhang Jhu, Liping Wang, Cho-Pei Jiang, and Cory J Xian. A hybrid platform for three-dimensional printing of bone scaffold by combin-

ing thermal-extrusion and electrospinning methods. *Microsystem Technologies*, 2019.

[53] Tao Xu, Kyle W Binder, Mohammad Z Albanna, Dennis Dice, Weixin Zhao, James J Yoo, and Anthony Atala. Hybrid printing of mechanically and biologically improved constructs for cartilage tissue engineering applications. *Biofabrication*, 5(1), 2012.

[54] Suresh Seethapathy and Tadeusz Gorecki. Applications of polydimethylsiloxane in analytical chemistry: A review. *Analytica Chimica Acta*, 750, 2012.

[55] Alvaro Mata, Aaron J Fleischman, and Shuvo Roy. Characterization of polydimethylsiloxane (pdms) properties for biomedical micro/nanosystems. *Biomedical Microdevices*, 7, 2005.

[56] Gianguido Baldinozzi, Yanwen Zhang, Katherine L Smith, and Kazuhiro Yasuda. Mater. res. soc. symp. proc. volume 1215 materials research needs to advance nuclear energy, 2010.

[57] DE Hanson. An explicit polymer and node network model to compute micromechanical properties of silica-filled polydimethylsiloxane. *Polymer*, 45(3), 2004.

[58] CJ Ani, JD Obayemi, VO Uzonwanne, Yiporo Danyuo, OS Odusanya, J Hu, K Malatesta, and WO Soboyejo. A shear assay study of single normal/breast cancer cell deformation and detachment from poly-di-methyl-siloxane (pdms) surfaces. *Journal of the Mechanical Behavior of Biomedical Materials*, 91, 2019.

[59] Germán Comina, Anke Suska, and Daniel Filippini. Pdms lab-on-a-chip fabrication using 3d printed templates. *Lab On A Chip*, 14(2), 2014.

[60] Sylgard^{TM} 184 datasheet: https://www.dow.com/content/dam/dcc/documents/en-us/productdatasheet/11/11-31/11-3184-sylgard-184-elastomer.pdf. accessed june 2023.

[61] Dowsil^{TM} 1700 datasheet: https://www.dow.com/en-us/document-viewer.html?docpath=/content/dam/dcc/documents/en-us/productdatasheet/11/11-17/11-1785-01-dowsil-se-1700-adhesive.pdf. accessed june 2023.

[62] Azzurra Volpi, Giovanni Cittadino, Alberto Di Lieto, Arlete Cassanho, Hans P Jenssen, and Mauro Tonelli. Investigation of yb-doped liluf4 single crystals for optical cooling. *Optical Engineering*, 56(1), 2017.

[63] Vetroalfa datasheet: https://www.filoalfa3d.com/upload/scheda/tds-vetroalfa-dec-2017.pdf. accessed june 2023.

[64] Jorge M Zuniga. 3d printed antibacterial prostheses. *Applied Sciences*, 8(9), 2018.

[65] Plactive^{TM} datasheet: https://formfutura.com/datasheets/copper3d-tds-plactive.pdf. accessed june 2023.

[66] Patrick F Flowers, Christopher Reyes, Shengrong Ye, Myung Jun Kim, and Benjamin J Wiley. 3d printing electronic components and circuits with conductive thermoplastic filament. *Additive Manufacturing*, 18, 2017.

[67] Graphene composite datasheet: https://3dcompare.com/materials/product/black-magic-3d-conductive-graphene-composite-1-75-mm/. accessed june 2023.

[68] Emo Chiellini, Andrea Corti, Salvatore D'Antone, and Roberto Solaro. Biodegradation of poly (vinyl alcohol) based materials. *Progress in Polymer Science*, 28(6), 2003.

[69] Q Fan. Fabric chemical testing. In *Fabric Testing*. Elsevier, 2008.

[70] MJ Snare, FE Treloar, KP Ghiggino, and PJ Thistlethwaite. The photophysics of rhodamine b. *Journal of Photochemistry*, 18(4), 1982.

[71] Ankita Jaisingh Sheoran and Harish Kumar. Fused deposition modeling process parameters optimization and effect on mechanical properties and part quality:

Review and reflection on present research. *Materials Today: Proceedings*, 21, 2020.

[72] John C de Mello, H Felix Wittmann, and Richard H Friend. An improved experimental determination of external photoluminescence quantum efficiency. *Advanced Materials*, 9(3), 1997.

[73] NC Greenham, IDW Samuel, GR Hayes, RT Phillips, YARR Kessener, SC Moratti, AB Holmes, and RH Friend. Measurement of absolute photoluminescence quantum efficiencies in conjugated polymers. *Chemical physics letters*, 241(1-2), 1995.

[74] Allan W Snyder, John D Love, et al. *Optical waveguide theory*, volume 175. Chapman and hall London, 1983.

[75] Max J Schnepf, Martin Mayer, Christian Kuttner, Moritz Tebbe, Daniel Wolf, Martin Dulle, Thomas Altantzis, Petr Formanek, Stephan Förster, Sara Bals, et al. Nanorattles with tailored electric field enhancement. *Nanoscale*, 9(27), 2017.

[76] Michele Gaio, Maria Moffa, Marta Castro-Lopez, Dario Pisignano, Andrea Camposeo, and Riccardo Sapienza. Modal coupling of single photon emitters within nanofiber waveguides. *ACS Nano*, 10(6), 2016.

[77] Antti Koski, Kate Yim, and SJML Shivkumar. Effect of molecular weight on fibrous pva produced by electrospinning. *Materials Letters*, 58(3-4), 2004.

[78] Schott optical glass datasheet: https://refractiveindex.info/download/data/2017/schott2017-01-20.pdf. accessed july 2023.

[79] Dhruv Saxena, Alexis Arnaudon, Oscar Cipolato, Michele Gaio, Alain Quentel, Sophia Yaliraki, Dario Pisignano, Andrea Camposeo, Mauricio Barahona, and Riccardo Sapienza. Sensitivity and spectral control of network lasers. *Nature Communications*, 13(1), 2022.

[80] Dan Li, Yuliang Wang, and Younan Xia. Electrospinning of polymeric and ceramic nanofibers as uniaxially aligned arrays. *Nano Letters*, 3(8), 2003.

[81] Jingwei Xie, Matthew R MacEwan, Wilson Z Ray, Wenying Liu, Daku Y Siewe, and Younan Xia. Radially aligned, electrospun nanofibers as dural substitutes for wound closure and tissue regeneration applications. *ACS Nano*, 4(9), 2010.

[82] Suk Hee Park and Dong-Yol Yang. Fabrication of aligned electrospun nanofibers by inclined gap method. *Journal of Applied Polymer Science*, 120(3), 2011.

[83] Halil İbrahim İçoğlu, Şirin Ceylan, Behzat Yıldırım, Mehmet Topalbekiroğlu, and Ali Kılıç. Production of aligned electrospun polyvinyl alcohol nanofibers via parallel electrode method. *The Journal of The Textile Institute*, 112(6), 2021.

[84] Suk Hee Park, Jung Woo Hong, Jennifer Hyunjong Shin, and Dong-Yol Yang. Quantitatively controlled fabrication of uniaxially aligned nanofibrous scaffold for cell adhesion. *Journal of Nanomaterials*, 2011, 2011.

[85] Zhenghai Tang, Yanda Lei, Baochun Guo, Liqun Zhang, and Demin Jia. The use of rhodamine b-decorated graphene as a reinforcement in polyvinyl alcohol composites. *Polymer*, 53(2), 2012.

[86] Mitsuo Kawasaki and Shuki Mine. Novel lasing action in dye-doped polymer films coated on large pseudotabular ag islands. *The Journal of Physical Chemistry B*, 110(31), 2006.

[87] L Allen and GI Peters. Amplified spontaneous emission and external signal amplification in an inverted medium. *Physical Review A*, 8(4), 1973.

[88] Andrea Camposeo, Francesca Di Benedetto, Ripalta Stabile, Antonio AR Neves, Roberto Cingolani, and Dario Pisignano. Laser emission from electrospun polymer nanofibers. *Small*, 5(5), 2009.

[89] M Anni, S Lattante, T Stomeo, R Cingolani, G Gigli, G Barbarella, and L Favaretto. Modes interaction and light transport in bidimensional organic random lasers in the weak scattering limit. *Physical Review B*, 70(19), 2004.

[90] Oleg Zaitsev, Lev Deych, and Vladimir Shuvayev. Statistical properties of one-dimensional random lasers. *Physical review letters*, 102(4), 2009.

[91] Y Ling, H Cao, AL Burin, MA Ratner, X Liu, and RPH Chang. Investigation of random lasers with resonant feedback. *Physical Review A*, 64(6), 2001.

[92] Xunya Jiang and CM Soukoulis. Time dependent theory for random lasers. *Physical review letters*, 85(1), 2000.